



Nina Fleischmann, BSc

A Polarization Entangled Photon Source with High Heralding Efficiency

MASTERARBEIT

zur Erlangung des akademischen Grades

Diplom-Ingenieurin

Masterstudium Technische Physik

eingereicht an der

Technischen Universität Graz

Betreuer

Univ.-Prof. Dipl.-Phys. Dr.rer.nat. Wolfgang Ernst

Institut für Experimentalphysik

ausgeführt am

Institut für Quantenoptik und Quanteninformation in Wien

Graz, November 2015

EIDESSTATTLICHE ERKLÄRUNG

Ich erkläre an Eides statt, dass ich die vorliegende Arbeit selbstständig verfasst, andere als die angegebenen Quellen/Hilfsmittel nicht benutzt, und die den benutzten Quellen wörtlich und inhaltlich entnommenen Stellen als solche kenntlich gemacht habe. Das in TUGRAZonline hochgeladene Textdokument ist mit der vorliegenden Masterarbeit identisch.

Datum

Unterschrift

Contents

1	Introduction	1
2	Fundamental Concepts of Quantum Theory	3
2.1	Polarization	3
2.2	State vector	5
2.3	Qubits	7
2.4	Entanglement	9
2.5	Nonlinear Optics	11
2.5.1	Spontaneous Parametric Down Conversion	11
2.5.2	Phase Matching	15
3	Sources of polarization entangled photons	19
3.1	Creation of an entangled state in a Sagnac-type source	20
4	Characterization Parameters	24
4.1	Optimizing Efficiency	27
5	High-heralding-efficiency Sagnac source	32
5.1	Architecture of the source	32
5.2	Source-Alignment procedure	35
5.3	Source Performance characteristics	38
5.3.1	Temperature setting	39
5.4	Heralding efficiency	39
5.5	Visibility	45
5.5.1	Visibility at higher single rates	48

Contents

6	Evaluation of phase stability	51
6.1	Performance with multi-mode-fibers	58
6.2	Performance with cross-spliced PM-fibers	60
7	Conclusion and Outlook	64
A	Appendix	66
A.1	Effects of accidental coincidences	66
A.2	Polarization flip with a cross-faced periscope	70
A.3	Alignment interferometer	71
A.4	Polarizing Beam Splitter	73
A.5	Polarization maintaining fibers	74
B	Error Analysis	75
	Bibliography	76
8	Acknowledgements	83

1 Introduction

In the early 20th century our understanding of physics was complemented by a striking new concept, the theory of quantum mechanics. Besides naturally raising philosophical questions about the fundamentals of nature, it has since led to applications that profoundly changed our daily life, such as lasers, transistors and LEDs amongst many others.

A rather recent field of application is the utilization of quanta inherent degrees of freedom for information processing. The quantum mechanical concepts of superposition and entanglement provide the basis of protocols for quantum computing, quantum enhanced metrology or quantum key distribution (QKD). In times where the secure transmission of digital data is of ultimate importance, especially the latter attracts more and more attention. However, presently commercially available QKD systems are based on distribution of entangled photons in optical fiber links, and thus are restrained to distances of a few hundred kilometers, due to fiber-related losses and decoherence-effects, as well as detector noise [1–4].

In order to establish a global-scale QKD-network, an alternative and utmost promising option is satellite-based distribution of photonic entanglement. This approach would not only allow for exceeding the distance limitations of optical fibers, its feasibility with state-of-the-art technology has already been proven by various experiments, employing horizontal long-distance free-space-links [5, 6] or an actual vertical space link [7]. Furthermore the space environment offers the opportunity for experiments in a novel and yet unexplored framework: the intersection of quantum mechanics and general relativity.

This thesis was done in course of developing a source for polarization entangled photons, that is suitable for space applications. Once implemented on a satellite, it is unaccessible, but still has to work reliably under harsher conditions than in any earth bound laboratory for the whole period of operation. Hence a space-suitable entangled photon source needs to fulfill special requirements, concerning size and mechanical stability (for example approached by [8]), power consumption, temperature stability and efficiency. The most promising candidate for meeting those requirements up to date is a Sagnac-type SPDC source in combination with type-II quasi phase matching.

In course of this thesis I built such a source and characterized it with respect to certain stability and efficiency demands. Special focus was laid on increasing the heralding efficiency, i. e. a high conditional probability of collecting both partners of an entangled photon pair in their conjugate optical fibers. Sources with high heralding efficiency are vital for any loss-sensitive applications, as it applies to an atmospheric optical link, but also for the first loophole free Bell test experiment.

2 Fundamental Concepts of Quantum Theory

This chapter shall give an introduction to the basic theory on which the experiments described in this thesis are resting upon.

2.1 Polarization

From Maxwell's equation of electromagnetic fields, we derive the following solution for the electric field:

$$\vec{E}(\vec{r}, t) = \vec{A} \times \exp [i(\vec{r}\vec{k} - \omega t)] \quad (2.1)$$

It describes a plane wave, that propagates in direction of the wave vector \vec{k} and oscillates perpendicular to \vec{k} with the amplitude A and the angular frequency $\omega = 2\pi\nu$. Without any loss of generality we define now the direction of propagation to be z . Analogous to a two-dimensional harmonic oscillator the time evolution of the field can be written as a superposition of two independent, orthogonal oscillations with the same frequency:

$$\vec{E}(z, t) = \vec{E}_x + \vec{E}_y = E_x \cdot \vec{e}_x + E_y \cdot \vec{e}_y \quad (2.2)$$

Polarization	φ	ϕ
Linear horizontal	0	0°
Linear vertical	0	90°
Linear diagonal	0	$+45^\circ$
Linear antidiagonal	0	-45°
Left handed circular	$+\pi/2$	-
Right handed circular	$-\pi/2$	-

Table 2.1: Nomenclature for basis polarization states.

with

$$\begin{aligned}
 E_x &= A_x \times \exp [i(\vec{r}\vec{k} - \omega t + \varphi_x)] \\
 E_y &= A_y \times \exp [i(\vec{r}\vec{k} - \omega t + \varphi_y)]
 \end{aligned}
 \tag{2.3}$$

If there exists a phase relation that is constant in time between \vec{E}_x and \vec{E}_y , i. e.

$$\vec{E} = \vec{E}_x + e^{i\varphi} \vec{E}_y, \quad \varphi = \varphi_x - \varphi_y = \text{const.}
 \tag{2.4}$$

then the light is said to be completely polarized. In general the field vector describes an ellipse in the x-y-plane, pictured in figure 2.1. It is characterized by its ellipticity $\epsilon = \pm \frac{b}{a}$, where positive values correspond to right-handed and negative ones to left-handed polarization, and the orientation angle ϕ , which describes the rotation of the major axis with respect to a chosen coordinate system. However, for $\varphi = 0$ or π the ellipse collapses to a line and the light is said to be linearly polarized. For $\varphi = \pm\pi/2$ the ellipse becomes a circle, therefore it is named circular polarization. Table 2.1 presents an overview of the states which are relevant to most quantum optics applications.

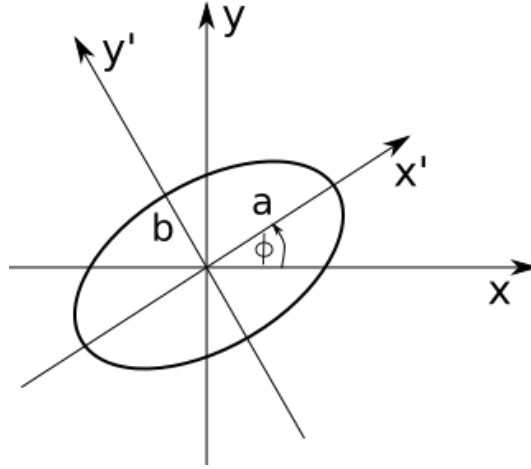


Figure 2.1: Polarization ellipse [9].

2.2 State vector

In quantum mechanics, using the Dirac notation, all information about a system is contained in the state vector

$$|\psi\rangle \in \mathcal{H}, \quad (2.5)$$

which is defined within a generally multidimensional Hilbert Space \mathcal{H} . This state is determined except for a phase factor and can be expanded in a set of orthonormal basis vectors

$$|\psi\rangle = \sum_i c_i |\phi_i\rangle \quad (2.6)$$

with the complex amplitudes c_i . Observable quantities are represented in this formalism with hermitian operators A :

$$A |\phi_i\rangle = a_i |\phi_i\rangle \quad (2.7)$$

where the eigenvalues a_i represent the possible outcomes of a measurement of A . By performing such a measurement we prepare the system in state $|\phi_i\rangle$, since every outcome a_i is attached only to one specific eigenstate $|\phi_i\rangle$ ¹. The probability that the result is a_i is given by the expectation value of A :

$$P(a_i) = \langle A \rangle = |\langle \phi_i | \psi \rangle|^2 = |c_i|^2 \quad (2.8)$$

Hence, a complete description of our system can be obtained by knowledge of the probability distribution, represented by the values c_i^2 . Each measurement updates our information about this distribution, but every single outcome is subject to a stochastic process [10]. Alternatively, the expectation value of an observable can be expressed as the trace over its corresponding operator A times the density matrix ρ :

$$\langle A \rangle = \text{tr}(A\rho) \quad (2.9)$$

In this equation the entire information about a system is stored in ρ . While all heretofore discussed descriptions correspond to pure states³, a system can also be in a mixed state, where coherent states $|\psi_i\rangle$ are incoherently superimposed with probabilities p_i :

$$\begin{aligned} \rho &= \sum_i p_i |\psi_i\rangle \langle \psi_i| \\ &= \sum_{i,j,k} p_i c_{ij} c_{ik}^* |\phi_j\rangle \langle \phi_k| \end{aligned} \quad (2.10)$$

1 This is usually referred to as the "collapse of the wavefunction" and only holds true for non-degenerate systems.

2 This is theoretically possible by measuring a complete set of observables A_i .

3 Described by the density matrix: $\rho = |\psi\rangle \langle \psi|$

with $\sum_i p_i = 1$. As $|\psi\rangle$ is a coherent superposition of states $|\phi\rangle$, a phase relation between the complex amplitudes exists, while it does not for the real valued coefficients p_i of a mixed state. Such a system can no longer be fully described, the only information obtainable is the probability with which it is observed in a certain pure state [11].

2.3 Qubits

Analogous to a classical binary digit (a "bit"), information can be stored within a two level quantum system, where the basis states of a two dimensional Hilbert space, $|0\rangle$ and $|1\rangle$, replace the logical 0 and 1 of the classical system. Such a quantum bit is referred to as "qubit". In contrast to the classical bit, a qubit does not have to be in either one of the states 0 or 1, it can also be in a coherent superposition of both. The most general description is therefore

$$|\psi\rangle = a|0\rangle + b|1\rangle, \quad (2.11)$$

with the normalized complex coefficients

$$|a|^2 + |b|^2 = 1. \quad (2.12)$$

Neglecting an overall phase factor, we can rewrite equation 2.11 in the following way:

$$|\psi\rangle = \cos\left(\frac{\theta}{2}\right)|0\rangle + e^{i\varphi}\sin\left(\frac{\theta}{2}\right)|1\rangle \quad (2.13)$$

with real valued variables θ and φ . They can be associated with the angles of a sphere with unit radius, commonly known as the "Bloch sphere". From illustration 2.2 it is evident, that every pure qubit state can be represented as a point on the surface of the sphere, whereas mixed states are located below the surface. The

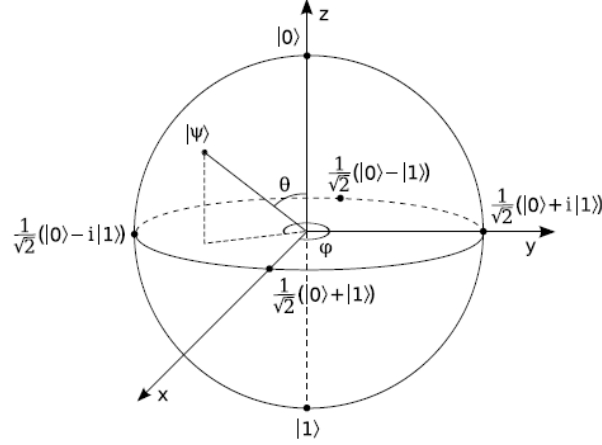


Figure 2.2: Arbitrary qubits $|\psi\rangle$ are commonly represented as coordinates on the Bloch sphere. Vectors with radius < 1 imply mixed states. The illustration is taken from [12].

three mutually unbiased bases for this system are marked on the poles and the equator.

Principally, the realization of a qubit can be achieved by the means of any quantum mechanical two-level system. The one most suited to free-space links and long distance transmission is encoding single photons, using for example their spatial, phase or polarization degrees of freedom, as well as arrival time or frequency [12]. The representation for polarization encoding, as used in this thesis, is listed in table 2.2. These states are eigenvectors of the Pauli matrices:

$$\sigma_x = \begin{pmatrix} 0 & 1 \\ 1 & 0 \end{pmatrix} \quad \sigma_y = \begin{pmatrix} 0 & -i \\ i & 0 \end{pmatrix} \quad \sigma_z = \begin{pmatrix} 1 & 0 \\ 0 & -1 \end{pmatrix} \quad (2.14)$$

with eigenvalues 1 and -1 (corresponding to the logical 0 and 1) respectively. By combination of these three Pauli-matrices and the identity-operator, any possible transformation within the two-dimensional Hilbert space can be generated. For polarization encoding this is customarily realized by the usage of wave-plates.

Qubit	Polarization
$ 0\rangle$	$ H\rangle$
$ 1\rangle$	$ V\rangle$
$\frac{1}{\sqrt{2}}(0\rangle + 1\rangle)$	$ D\rangle$
$\frac{1}{\sqrt{2}}(0\rangle - 1\rangle)$	$ A\rangle$
$\frac{1}{\sqrt{2}}(0\rangle + i 1\rangle)$	$ L\rangle$
$\frac{1}{\sqrt{2}}(0\rangle - i 1\rangle)$	$ R\rangle$

Table 2.2: Polarization representation of the three mutually unbiased bases on the Bloch sphere. The letters indicate horizontal (H), vertical (V), diagonal (D) and antidiagonal (A) linear polarization, as well as left-handed (L) and right-handed (R) circular polarized light, similar to classical representations on the Poincaré-sphere (see for example [9]).

2.4 Entanglement

The previously presented formalism can be extended to an arbitrary number of qubits. However, the essential characteristics of such combined systems can already be demonstrated for two subsystems, as they will be of main importance within this thesis, and we will therefore restrict theoretical contemplations to them.

As pointed out before, two systems A and B can be described in their respective Hilbert space:

$$|\psi\rangle_A \in \mathcal{H}_A, \quad |\psi\rangle_B \in \mathcal{H}_B \quad (2.15)$$

The composite system is then embedded in the tensor product of both sub-spaces:

$$\mathcal{H}_{AB} = \mathcal{H}_A \otimes \mathcal{H}_B \quad (2.16)$$

Every state in this product space can now be expanded in a linear combination of orthonormal product states:

$$|\psi\rangle_{AB} = \sum_{i,j} \alpha_{i,j} |\phi_i\rangle_A |\phi_j\rangle_B \quad (2.17)$$

with $|\phi_i\rangle_A$ and $|\phi_j\rangle_B$ being the basis vectors of the respective subsystems A and B and $\alpha_{i,j}$ complex amplitudes. It is now evident that any product of the subsystems is an element of the composite Hilbert space, but in return not every element of this Hilbert space can be written as a product of the two subsystems,

i. e.

$$|\psi\rangle_{AB} \neq |\psi\rangle_A \otimes |\psi\rangle_B \quad (2.18)$$

If this factorization is not possible, the state is called *entangled*. This expression was originally introduced by E. Schrödinger as "*Verschränkung*"⁴ in the second of his two famous articles about quantum mechanics in 1935 [10]. Here he refers to the direct consequence of the formalism, that the information obtainable about the individual systems is conditioned, thus only the information about the total system can be maximal.

This is best demonstrated with the four maximally entangled Bell states⁵:

$$|\psi^\pm\rangle_{12} = \frac{1}{\sqrt{2}} (|H\rangle_1 |V\rangle_2 \pm |V\rangle_1 |H\rangle_2) \quad (2.19)$$

$$|\phi^\pm\rangle_{12} = \frac{1}{\sqrt{2}} (|H\rangle_1 |H\rangle_2 \pm |V\rangle_1 |V\rangle_2) \quad (2.20)$$

here shown in the polarization basis for two photons, indicated with 1 and 2. Maximally entangled is to be comprehended as occurrence of strict anticorrelation or

4 Or more explicitly "*Verschränkung der Voraussagen*" or "*Verschränkung unseres Wissens um... [zwei] Körper*", which may be translated to "entanglement of predictions" or "entanglement of our knowledge" about two particles.

5 Named after J. S. Bell, mostly famous for his inequality to rule out any hidden variable model in quantum mechanics [13].

correlation⁶. Upon performing a polarization measurement on either photon 1 or 2, we can forecast the state of the other with unit probability, yet predictions for each individual measurement outcome are impossible.

2.5 Nonlinear Optics

If an optical light field propagates through a non-centrosymmetric material, it induces a polarization response that is in general proportional to the field-strength and described by a tensor $\chi^{(1)}$. However, if the incoming field reaches strengths that are comparable with the interatomic fields⁷, then also nonlinear interactions can occur. This behaviour is described via a Taylor expansion of the polarization:

$$P_i = \epsilon_0(\chi_{ij}^{(1)} E_j + \chi_{ijk}^{(2)} E_j E_k + \chi_{ijkl}^{(3)} E_j E_k E_l + \dots) \quad (2.21)$$

where ϵ_0 is the vacuum permittivity and the tensor $\chi^{(n)}$ is n^{th} order susceptibility with rank $n+1$. The interaction of multiple fields can give rise to frequency conversion, where $\chi^{(2)}$ -interactions correspond to 3-wave-mixing processes, $\chi^{(3)}$ -interactions to 4-wave-mixing processes, and so on.

In the following only interactions in which one pump field is converted into two output fields, under conservation of energy and momentum, will be considered.

2.5.1 Spontaneous Parametric Down Conversion

Spontaneous Parametric Down Conversion (SPDC) is such a 3-wave-mixing process and today the most common method to produce single heralded and entan-

⁶ It is to note though, that only the anticorrelation of $|\psi^-\rangle$ is invariant under rotation.

⁷ These strengths are usually in the order of $10^5 - 10^8$ V/m and can be achieved by laser-emission [14].

gled photons. A pump photon is interacting with a nonlinear medium and thus converted into a pair of photons with lower frequency, designated as signal and idler.

This process cannot be explained fully classical and we might therefore switch to a quantum mechanical approach. Here the down converted fields are initially in their respective vacuum states, and these vacuum fluctuations are amplified by nonlinear interaction with a pump field. It is described by an interaction Hamiltonian

$$\hat{H}_{SPDC} \propto \int_V dV \chi^{(2)} \hat{E}_p^{(+)}(\vec{r}, t) \hat{E}_s^{(-)}(\vec{r}, t) \hat{E}_i^{(-)}(\vec{r}, t) + h.c. \quad (2.22)$$

where p labels the pump, s the signal and i the idler field respectively and the interaction is assumed to only take place in a restricted volume V. The electric field operators can be expanded in plane waves of the form

$$\hat{E}_j^{(+)} = \hat{E}_j^{(-)\dagger} = A \int d^2\vec{q}_j d\omega_j e^{i(\vec{k}_j(\omega_j)\vec{r} - \omega_j t)} \hat{a}_j(\omega_j) \quad (2.23)$$

with $j = p, s, i$ designating pump, signal and idler. The vector \vec{q} denotes the transverse component of the wavevector $\vec{k}_j(\omega_j)$ and $\hat{a}_j(\omega_j)$ the annihilation operator for frequency ω_j and wavevector $\vec{k}_j(\omega_j)$. All constants are combined in the prefactor A. Since the strong pump field is almost not depleted by the nonlinear interaction, it is suitable to treat it as a classical field:

$$E_p^{(+)} = E_p^{(-)*} = \int d\omega_p \alpha(\vec{q}_p, \omega_p) e^{i(\vec{k}_p(\omega_p)\vec{r} - \omega_p t)} \quad (2.24)$$

where the function $\alpha(\vec{q}_p, \omega_p)$ is replacing the annihilation operator and characterizes amplitude, spatial and spectral distribution of the pump field.

In the Schrödinger picture the evolution of the photons is described as the time evolution of their state vector:

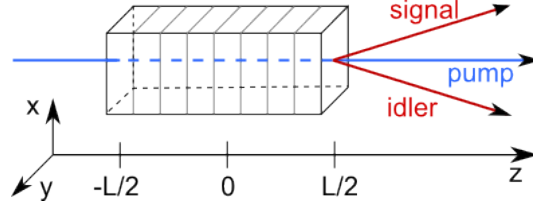


Figure 2.3: The coordinate system used for the calculations. The pump is propagating along the z-axis and its phase is considered zero at the center of the crystal.

$$|\psi(t)\rangle = e^{-\frac{i}{\hbar} \int_{t_0}^t dt' \hat{H}(t')} |\psi(t_0)\rangle \quad (2.25)$$

We presume that the down converted photons are initially in the vacuum state, i.e. $|\psi(t_0)\rangle = |vac\rangle_s |vac\rangle_i$. For a weak nonlinear interaction and maximal emission of one photon pair, one can obtain a proper description by just looking at the first order solution for a perturbation expansion on state (2.25):

$$|\psi(t)\rangle \approx |vac\rangle - \frac{i}{\hbar} \int_{t_0}^t dt' H(t') |vac\rangle_s |vac\rangle_i \quad (2.26)$$

Higher order terms correspond to multi-photon-pair-emission and are neglected within this derivation⁸. The calculations can be simplified by the choice of a convenient coordinate system. Hence in the following we assume the crystal with length L in the center of our coordinate system, with the pump beam propagating along the z-direction, as illustrated in figure 2.3. After inserting equations (2.22)-(2.24) into (2.26) the state reads

$$\begin{aligned} |\psi(t)\rangle \approx |vac\rangle - \frac{i}{\hbar} B \int_{t_0}^t dt' \iiint_{\omega} d\omega_p d\omega_s d\omega_i \alpha(\vec{q}_p, \omega_p) \int_z dz \iint_{\vec{p}} d\vec{p} \\ \times e^{-i(\omega_p - \omega_s - \omega_i)t'} e^{i(k_p^z - k_s^z - k_i^z)z} e^{i(\vec{q}_p - \vec{q}_s - \vec{q}_i)\vec{p}} \\ \times \hat{a}_s^\dagger(\omega_s) \hat{a}_i^\dagger(\omega_i) |vac\rangle_s |vac\rangle_i + h.c. \end{aligned} \quad (2.27)$$

⁸ For a more detailed contemplation of the topic the reader is referred to [15] or [16].

where the integration over the interaction volume is separated into an integral along the propagation axis and an integral over the transverse dimensions, with $\vec{\rho}$ and \vec{q} denoting the transversal position- and wavevector. All constants are combined in the prefactor B. The integration boundaries in the longitudinal dimension are determined by the crystal length and stretch from $-\frac{L}{2}$ to $\frac{L}{2}$. Due to the fact that the interaction-cross-section of the crystal is usually very large compared to the transverse expansions of the beam, we can extend the bounds in the x-y-directions from $-\infty$ to ∞ , which results in a delta-function for the transverse momenta:

$$\iint_{-\infty}^{\infty} d\vec{\rho} e^{i(\vec{q}_p - \vec{q}_s - \vec{q}_i)\vec{\rho}} \rightarrow 2\pi\delta(\vec{q}_p - \vec{q}_s - \vec{q}_i) \quad (2.28)$$

Taking into account that the interaction only occurs for a non-zero pump field, for the Hamiltonian being non-zero then, we are able to stretch the time integration boundaries from $t_0 = -\infty$ to $t = \infty$:

$$\int_{-\infty}^{\infty} dt' e^{-i(\omega_p - \omega_s - \omega_i)t'} \rightarrow 2\pi\delta(\omega_p - \omega_s - \omega_i) \quad (2.29)$$

By also taking into account the polarization of the electric fields we finally arrive at

$$|\psi\rangle = |vac\rangle - B' \int d\vec{q}_s d\vec{q}_i d\omega_s d\omega_i \Phi(\vec{q}_s, \vec{q}_i, \omega_s, \omega_i) \times \hat{a}_s^\dagger(\omega_s) \hat{a}_i^\dagger(\omega_i) |vac\rangle_s |vac\rangle_i \quad (2.30)$$

where all constants are combined in the prefactor B', which is proportional to the length of the crystal L and the strength of the pump field E_p . The spectral shape of the final state is given by the biphoton amplitude:

$$\Phi(\vec{q}_s, \vec{q}_i, \omega_s, \omega_i) = \alpha(\vec{q}_s + \vec{q}_i, \omega_s + \omega_i) \times \text{sinc}(\Delta k^z \frac{L}{2}) \quad (2.31)$$

where $\Delta k^z = k_p^z(\vec{q}_s + \vec{q}_i, \omega_s + \omega_i) - k_s^z(\vec{q}_s, \omega_s) - k_i^z(\vec{q}_i, \omega_i)$ indicates the phase mismatch.

2.5.2 Phase Matching

Equation (2.31) implies that efficient SPDC is only possible for $\Delta k^z = 0$. Otherwise destructive interference of the signal and idler waves will prevent the mode amplitudes from growing. Together with equations (2.29) and (2.28) we arrive at following relations, ensuring conservation of energy and momentum and thus the parametric interaction:

$$\vec{k}_p = \vec{k}_s + \vec{k}_i \quad (2.32)$$

$$\omega_p = \omega_s + \omega_i \quad (2.33)$$

Those are in general not fulfilled at the same time in a dispersive medium where $k = \frac{n(\omega)\omega}{c}$. However, in anisotropic bulk crystals the fields experience refractive indices that are dependent on their polarization, the temperature and their relative angle to the optical axis of the crystal⁹:

$$\Delta k^z = \frac{n_{\vec{e}_p}(\omega_p, T, \theta_p)}{c_0} \omega_p - \frac{n_{\vec{e}_s}(\omega_s, T, \theta_s)}{c_0} \omega_s - \frac{n_{\vec{e}_i}(\omega_i, T, \theta_i)}{c_0} \omega_i \quad (2.34)$$

with $\vec{e}_{p,s,i}$ the polarization vector, T being the temperature and $\theta_{p,s,i}$ the angle between wave vector and optical axis of the crystal for each field. By choosing the waves to be orthogonally polarized and adjusting all other parameters accordingly, the phase matching conditions can be satisfied. With the labels extraordinary (e) for the polarization vector being within the principal plane¹⁰ and ordinary

⁹ Those relations are described for different materials by the empirical Sellmeier equations. Measurements for ppKTP were derived inter alia in [17].

¹⁰ The principal plane is the plane spanned by the pump vector and the optical axis of the crystal.

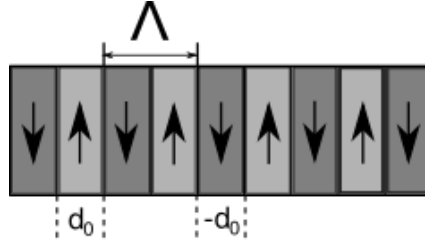


Figure 2.4: Illustration of a periodically poled crystal with grating period Λ and alternating nonlinear coefficient d_0 .

(o) for the polarization vector being orthogonal to it, we categorize as follows [15]:

- **Type-0:** pump (e) \rightarrow signal (e) + idler (e)
- **Type-I:** pump (e) \rightarrow signal (o) + idler (o)
- **Type-II:** pump (e) \rightarrow signal (e) + idler (o)

In general, at least one of the generated fields propagates in a direction that does not coincide with a principal axis of the birefringent nonlinear crystal. In this case the Poynting vector walk-off between the fields generated in different regions of the crystal no longer overlap, which limits the maximum permissible crystal length (*critical phase-matching*). A configuration in which the fields propagate along a principal axis is known as a *non-critical phase-matching* condition. In general this requires periodic poling of the crystal's nonlinearity.

A method that offers more freedom in customizing the SPDC states is called *quasi phase matching* (QPM) and was first introduced in [18]. The concept is to shape the nonlinear properties of a crystal in a way that allows for phase matching with the desired angles $\theta_{p,s,i}$ and frequencies $\omega_{p,s,i}$. The most common implementation is enabling collinear emission in a periodically poled crystal. Due to the sinc-function in equation (2.31) the down converted waves would interfere destructively after a crystal length $L_c = \frac{2\pi}{\Delta k}$, the so called "coherence length". By alternating the sign of the nonlinear coefficient along the propagation direction after a grating period

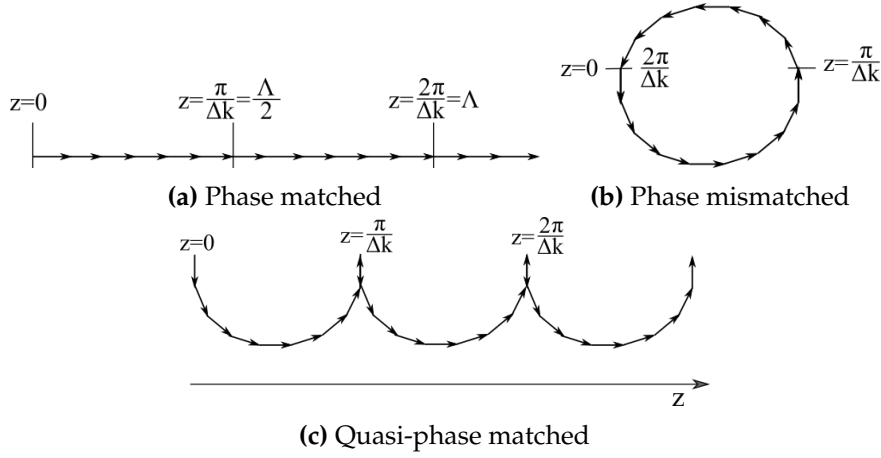


Figure 2.5: Three possibilities for mode-development insight the crystal. Figure reproduced from [14].

$\Lambda = L_c$, effective mode growing can be achieved. This is illustrated in figures 2.4 and 2.5 and expressed in the condition for QPM:

$$\Delta k^z = k_p^z - k_s^z - k_i^z - \frac{2\pi}{\Lambda} \quad (2.35)$$

Periodic poling significantly reduces the effort with which perfect quasi phase matching can be achieved in experiment, and has led to some of the brightest sources of photon pairs demonstrated to date.

The generation of photon pairs which are entangled in their polarization degree of freedom usually demands some additional effort. In general polarization-entanglement requires the coherent superposition of two pair-creation possibilities, which generate orthogonally polarized photons. The most general superposition state, which includes the spatial-temporal correlations intrinsic to the SPDC process is:

$$|\psi\rangle = \frac{1}{\sqrt{2}} \int d\omega_s d\vec{q}_s d\omega_i d\vec{q}_i (\Phi_{HV}(\omega_s, \vec{q}_s, \omega_i, \vec{q}_i) \hat{a}_H^\dagger(\omega_s) \hat{a}_V^\dagger(\omega_i) + \Phi_{VH}(\omega_s, \vec{q}_s, \omega_i, \vec{q}_i) \hat{a}_V^\dagger(\omega_s) \hat{a}_H^\dagger(\omega_i)) |vac\rangle_s |vac\rangle_i \quad (2.36)$$

Only if the spatio-temporal parts of the wavefunctions overlap perfectly, i. e.

$$\Phi_{HV}(\omega_s, \vec{q}_s, \omega_i, \vec{q}_i) = \Phi_{VH}(\omega_s, \vec{q}_s, \omega_i, \vec{q}_i) \quad (2.37)$$

the polarization part factorizes out:

$$|\psi\rangle \propto \int d\omega_s dq_s d\omega_i dq_i \dots |\vec{q}_s, \omega_s\rangle |\vec{q}_i, \omega_i\rangle \otimes (|H\rangle_s |V\rangle_i + e^{i\phi} |V\rangle_s |H\rangle_i) \quad (2.38)$$

The overlap of the spatio-temporal wavefunctions is entirely equivalent to the requirement of temporal and spectral indistinguishability of the two pair-generation processes. In general this requires timing compensation crystals. In the following we discuss a simple manner in which this indistinguishability is automatically ensured by employing only a single nonlinear crystal placed inside a Sagnac loop.

3 Sources of polarization entangled photons

The priorly discussed mechanisms of nonlinear optics provide a very convenient way to produce single photons and entangled photon pairs. This chapter shall introduce the reader to the experimental implementation of SPDC in a nonlinear crystal in a source for polarization entangled photons. The focus is laid on the design that is used for this thesis.

There are different concepts for implementing a nonlinear crystal in an entangled photon source. Early approaches used β -barium borate (BBO) crystals with type-II [19] or type-I phase matching [20], which still suffered from a trade off between high flux and spatial distinguishability of the output modes. This disadvantage could be overcome with the utilization of periodically poled bulk crystals, such as ppKTP or ppLN, which allow for collinear emission of the downconverted photons (see section 2.5.2). The sources are usually making use of double- [21] or single-crystal geometries [22], whereby schemes that exploit interferometer architectures, as introduced in [23, 24], turn out to be especially convenient for most applications.

The source used in this thesis is based on the Sagnac-interferometer design, but with a polarizing beam splitter (PBS) instead of a conventional 50/50 beam splitter. It is making use of type-II quasi phase matching within a ppKTP, which is placed in the center of the interferometer and pumped from both sides with linearly polarized light. The functional principle will be explained in the following.

3.1 Creation of an entangled state in a Sagnac-type source

An illustration and explanation of the functioning principle of the Sagnac interferometer source is given in figure 3.1, but will also be explained in the following text.

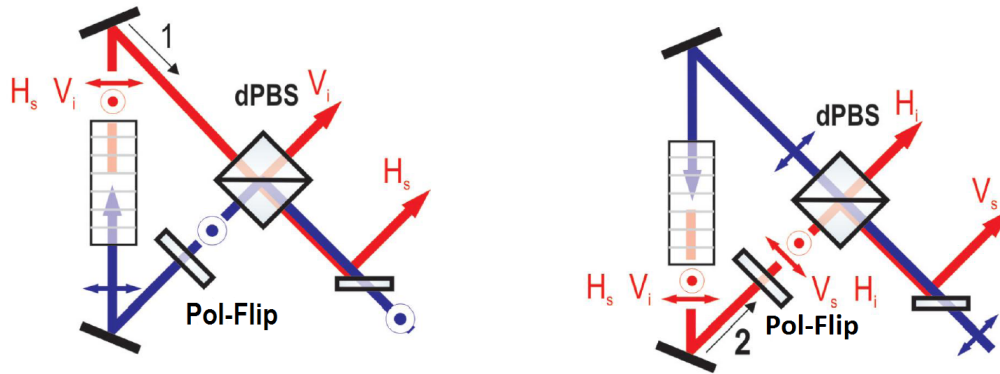
As pointed out before, the source can be pumped in both directions. By sending in diagonally polarized light, it is half reflected by the PBS and half transmitted, therefore it enters the crystal from both sides with equal intensity. The vertically polarized component is reflected at the PBS and traverses the Sagnac loop in a clockwise sense (see figure 3.1a). The polarization is changed by a cross-faced periscope (labeled as "Pol-Flip"), that interchanges H- and V-polarization of the pump light¹. Thus the pump enters the ppKTP aligned to its phase matched axis and with a certain probability a down converted photon pair is created. The two photons of the pair are designated as signal and idler respectively, according to their horizontal or vertical polarization. Signal and idler are then separated at the PBS into modes 3 and 4 and can be collected independently. The horizontal component of the pump light traverses the loop in a counterclockwise sense (see figure 3.1b). Now the polarization of the down converted photons is interchanged by the "Pol-Flip", so the signal exits the PBS with vertical polarization in mode 3 and the idler with horizontal in mode 4. The overlap of both loops is pictured in 3.1c.

Assuming equal SPDC-efficiencies for both pump directions, the superimposed state after the PBS for photon pairs arriving from both directions is proportional to

$$|\psi\rangle \propto \frac{1}{\sqrt{2}}(|H_i\rangle_3 |V_s\rangle_4 + e^{i\phi} |V_i\rangle_3 |H_s\rangle_4) \quad (3.1)$$

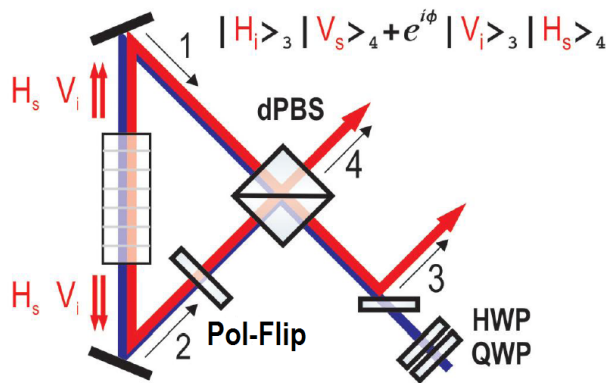
The phase ϕ is independent of the path lengths between crystal center and PBS and is determined only by an offset phase, which the photons obtain by traversing the

¹ A derivation of the polarization flipping effect is given in A.2.



(a) The V-polarized pump light is reflected at the PBS and propagates clockwise within the Sagnac loop. A periscope (labeled as "Pol-Flip") interchanges V- and H-polarization, so the now H-polarized pump enters the crystal aligned to its optical axis. The signal photon carries the same polarization as the pump and is transmitted at the PBS, whereas the idler photon is V-polarized and reflected.

(b) By pumping the source with H-polarized light, an inverse situation to (a) is created: the pump is now transmitted at the PBS and propagates counterclockwise within the Sagnac loop. The polarization of the down converted photons is flipped by the periscope and now the idler leaves the PBS H-polarized and the signal V-polarized.



(c) By sending in diagonally polarized light, the Sagnac loop is pumped bidirectionally. After the PBS a superimposed state of both possibilities (the signal being either H or V, and likewise for the idler) is created.

Figure 3.1: Illustration of the working scheme of the Sagnac interferometer type source. The pictures are taken from [25]

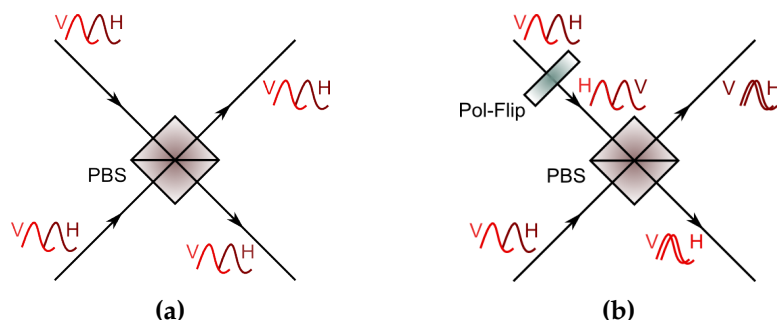


Figure 3.2: Scheme of the Sagnac walk-off autocompensation. In figure (a) no Pol-Flip is implemented, thus signal and idler are distinguishable in timing (illustrated with one wave being ahead of the other), but also in wavelength for non-degenerate SPDC (illustrated by the dark and light red colors). In figure (b) the polarizations are flipped in one arm and signal and idler modes carry no information about their origin anymore.

periscope and PBS (labeled with $\theta_{p,s,i}$ for pump, signal and idler respectively), plus the initial phase of the pump ϕ_p :

$$\phi = \theta_p + \theta_s - \theta_i - \phi_p \quad (3.2)$$

By compensating the offset phase of the interferometer with a waveplate that is tilted appropriately, the phase of the output state is solely determined by the pump. One can now adjust ϕ_p to be either 0 or π by setting the pump polarization to be diagonal (D) or antidiagonal (A). The first option would result into a $|\psi^-\rangle$ -state and the second into a $|\psi^+\rangle$ -state.

Creating the maximally entangled state in (3.1) is only possible for bidirectional pumping and elimination of all relations between polarization and any other degrees of freedom. As illustrated in figure 3.2, this already happens automatically within the Sagnac-scheme as a natural consequence of its symmetric architecture.

Due to the birefringence of the ppKTP-crystal the H- and V-polarized photons travel at different group velocities. This results in a temporal delay between the two modes, that is determined by the position of creation inside the crystal. Furthermore, in the

case of non-degenerate SPDC, the photons will always emerge with a wavelength related to their polarization (compare with figure 3.2a). By flipping the polarization in one arm (figure 3.2b), the spectral/temporal information is dis-entangled from the polarization entanglement. The priorly faster H-polarized photon is now V-polarized and exits the PBS in the same mode as the faster H-photon of the other pair, likewise for the idler-photons. It is now impossible to make conclusions about the polarization from the arrival time. Also any wavelength-relations are eliminated, since the signal photons will always exit the PBS at the same port, as well as the idler.

4 Characterization Parameters

To be able to compare different sources for entangled photons, parameters are used that characterize the efficiency of pair-production and the quality of the output entangled state. Some, which are of interest within this thesis, will be discussed in the following.

- **Degree of entanglement:**

For the majority of applications, as QKD or Bell tests, a high degree of entanglement must be guaranteed. To measure how much entanglement an experimentally generated state actually inherits, one can use different methods. Most of them quantify the conformity of the prepared state with a target state.

The quantum visibility of the correlation function provides an experimentally easily applicable method. Analogue to the classical interference visibility (or fringe visibility), it quantifies the contrast of the probability interference of the biphoton wave:

$$V = \frac{R_{c,max} - R_{c,min}}{R_{c,max} + R_{c,min}} \quad (4.1)$$

with R_c being the coincidence counts one encounters in a joint polarization measurement of the photon pairs. In practice this can be realized by the photons traversing two separate polarizers. The conditional probability that both photons pass, and therefore the coincidence count rate, is dependent on the polarizer settings. For the anticorrelated $|\psi^-\rangle$ -state it follows a \sin^2 -function:

$$R_c(\alpha, \beta) \propto \sin^2(\alpha - \beta) \quad (4.2)$$

with α and β being the angle settings of the respective linear polarizers. However, it is notable that a visibility of 1 not always yields an entangled state. This outcome can also be measured for a product state in its computational basis. Therefore it is necessary to measure at least in two conjugate bases, for example H/V- and D/A. For photon pairs that originate from a parametric down conversion process though, $V > 50\%$ ensures entanglement [25].

One can also derive a so called Bell-state-fidelity, as elaborated in [26]. A more sophisticated way to determine the amount of entanglement in a given system is provided by a full state tomography, as proposed for example in [27].

- **Pair collection probability**

The pair collection probability is given by the overlap integral of the signal and idler phase-matched mode-functions and the mode of their conjugate fiber:

$$P_{si} = \int d\vec{q} \Phi(\omega_s, \omega_i, \vec{q}_s, \vec{q}_i) \times E_s(\omega_s, \vec{q}) \times E_i(\omega_i, \vec{q}) \quad (4.3)$$

with $E_{s,i}$ being fundamental Gaussian modes of the signal and idler single-mode-fibers, with their waists $w_{s,i}$ located at the tip of the fiber:

$$E_j = \frac{w_j}{\sqrt{2\pi}} \times \exp\left(-w_j^2 \frac{(q_x^2 + q_y^2)}{4}\right) \quad (4.4)$$

Equation (4.3) represents the probability of collecting the partner photons in their respective optical fibers any given pump photon. It is equivalent to the experimentally observed coincidence rate R_c .

- **Heralding efficiency:**

The heralding efficiency $\eta_{s(i)}$ is the conditional probability that the signal (or idler) photon is collected, if its partner already coupled into the conjugate fiber (in general a single mode fiber):

$$\eta_{s(i)} = \frac{P_{si}}{P_{s(i)}} = \frac{R_c}{R_{s_{s(i)}}} \quad (4.5)$$

$P_{s(i)}$ are the probabilities to emit one signal (idler) photon into the collection mode (in general a Gaussian), independent of its partners properties. It is the sum over the joint collection probabilities with the partner photon being in a different spatial mode, which is the sum over all spatial modes the partner photon could be in. $\eta_{s(i)}$ is equivalent to the experimentally observed ratio of coincidences (R_c) to singles ($R_{s_{s(i)}}$).

It is notable that due to the spatial correlations a signal photon in a non-optimal Gaussian mode projects the idler onto a mode that is not a Gaussian and will not couple well to a Gaussian collection mode of any size.

- **Spectral bandwidth:**

The SPDC process in bulk media is tolerant to a certain phase mismatch, which corresponds to an uncertainty in the wave vector. As explained in section 2.5.2 the length of the interaction volume L is limited to a finite value $|\Delta k| \leq \frac{2\pi}{L}$ for a positive energy flow. Due to energy conservation, i. e. $\omega_p = \omega_s + \omega_i$, small deviations $\Delta\omega$ from the center frequency are allowed, if they satisfy phase matching at the same time:

$$|\Delta k(\omega_p, \omega_s + \Delta\omega, \omega_i - \Delta\omega)| \leq \frac{2\pi}{L} \quad (4.6)$$

The bandwidth of the down conversion therefore depends on the phase matching configuration and the crystal length L . For type-II quasi phase matching it is mainly dependent on the group dispersion in the crystal:

$$\Delta\omega_s = \Delta\omega_i \sim \frac{2\pi c}{|N_s - N_i|} \frac{1}{L} \quad (4.7)$$

with $N_{s,i}$ the refractive group indices of the collection modes. Expressing the bandwidth in terms of wavelength, the full width half maximum (FWHM) of signal and idler spectra can be approximated as follows [28]:

$$\Delta\lambda_{s,i,FWHM}[nm] \sim \frac{5.52}{L[mm]} \quad (4.8)$$

This equation is valid for ppKTP type-II phase matching at a signal and idler center wavelength of $\lambda_{s,i} = 810$ nm.

- **Spectral brightness:**

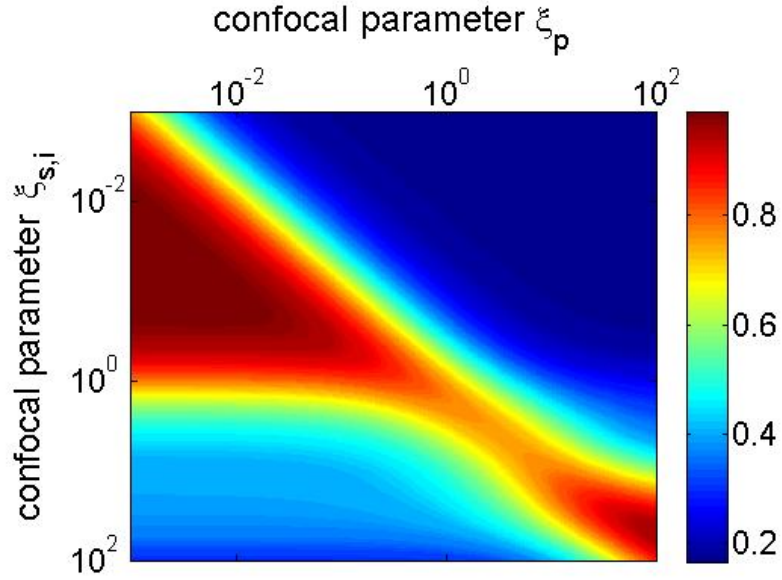
The Spectral brightness is the probability to emit and collect a photon pair into a specified mode per nm bandwidth, per mW pump power. It is usually experimentally approximated by the observed coincidences (minus accidentals), divided by the spectral FWHM bandwidth of the SPDC $\Delta\lambda$, the integration time t_{meas} and the pump power P_{pump} :

$$B = \frac{R_c}{\Delta\lambda \cdot t_{meas} \cdot P_{pump}} \quad (4.9)$$

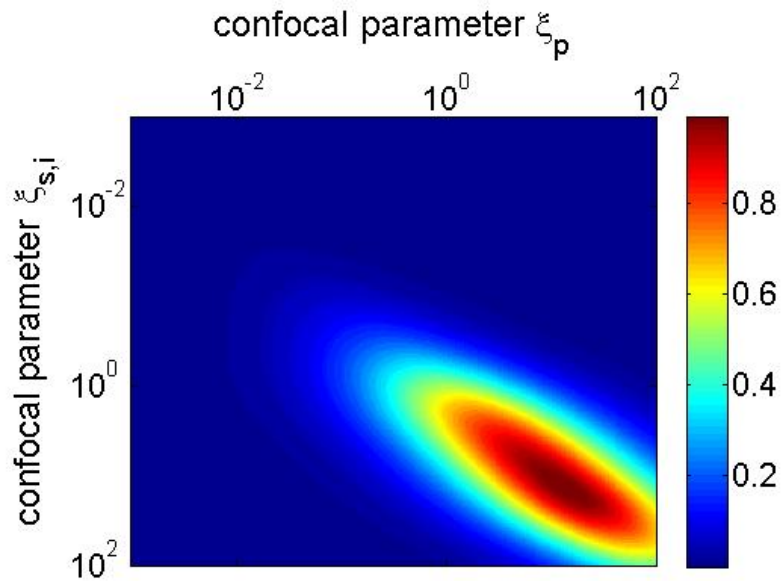
For ppKTP type-II collinear down conversion the spectral brightness scales as $B \sim L$ [29].

4.1 Optimizing Efficiency

For various applications it is desirable to tailor the previously depicted efficiency parameters according to certain requirements. In general those are high visibility for all applications that require a low QBER (such as QKD and Bell-test experiments),

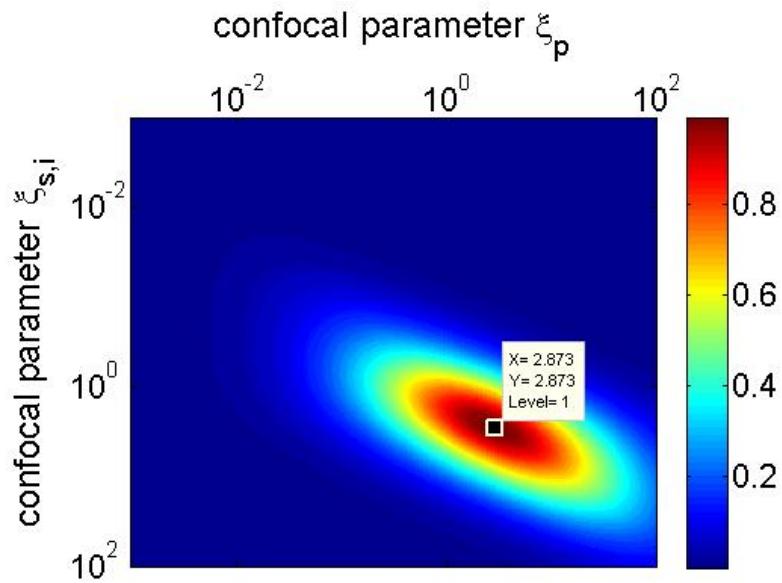


(a) Heralding efficiency as a normalized function of pump and collection confocal parameter.

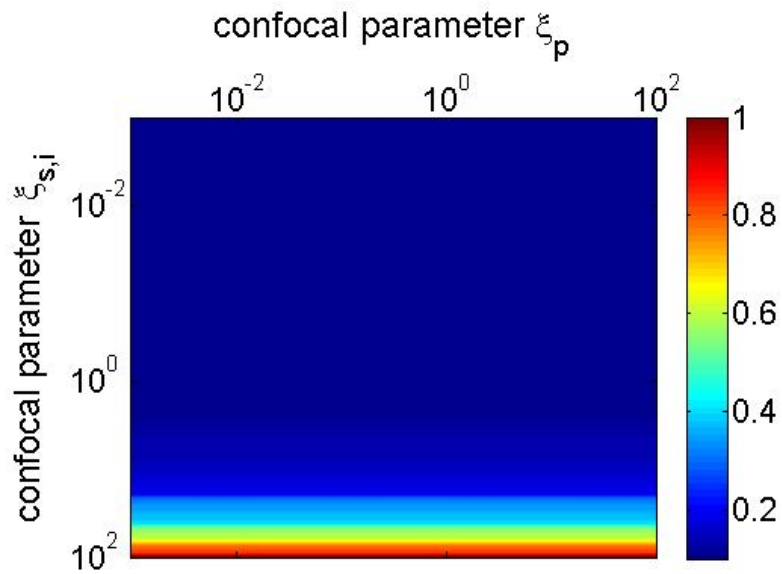


(b) Normalized pair collection efficiency per pump photon as function of pump and collection confocal parameter.

Figure 4.1: Characterization parameters. Heralding efficiency and pair collection efficiency cannot be optimized at the same time.



(a) Spectral brightness as a normalized function of pump and collection confocal parameter. The maximizing parameters are already known from Boyd and Kleinman [30].



(b) Normalized SPDC-bandwidth as a function of pump and collection confocal parameter.

Figure 4.2: Characterization Parameters.

high brightness and heralding efficiency for loss-sensitive applications, or broad bandwidths for experiments where short correlation times are of interest (for example time-bin-entanglement) and small bandwidths for long coherence times (for example for quantum information storage [31]).

It can be shown that the visibility for a given single count rate can be increased by a higher heralding efficiency (see section A.1). This again demands efficient coupling of the SPDC modes into optical fibers. The spatial mode that is emerging from laser resonators and is supported by usual single mode fibers can be approximated by a fundamental Gauss-mode¹. Hence, the operation of the SPDC source with Gaussian beams comes naturally. Various studies that address this topic (for example [29, 32, 33]) show that, for photon pairs created via bulk-SPDC, the spectral and spatial properties depend strongly on the focusing of the pump and collection modes into the crystal. This is typically expressed in terms of the dimensionless confocal parameter

$$\zeta = \frac{L}{2z_R} \quad (4.10)$$

where L is the length of the crystal and $z_R = \omega_0^2 \pi n / \lambda$ the Rayleigh-range. A small confocal parameter corresponds to weak focusing and $\zeta > 1$ to strong focusing. By choosing parameters that maximize the overlap of the signal and idler modes with the mode of the optical fiber, the coupling efficiency can be increased. Such optimal parameters ζ_{opt} can be derived for arbitrary crystal lengths.

The dependencies of the heralding efficiency, pair-collection efficiency, spectral brightness and spectral bandwidth on the pump and collection confocal parameter are illustrated in figures 4.1 and 4.2². For the calculations the same confocal parameter for signal and idler were assumed. This results in an independence of the bandwidth from the pump focus. Without any further filtering solely the crystal properties and the mode field of the collection optics limit the bandwidth. Tight focusing

¹ For further information the reader is referred to [9, 14].

² The calculations have been performed with MATLAB by my colleague Fabian Steinlechner and are analogue to those introduced in [29].

allows to collect more transverse plane wave components, therefore the bandwidth increases.

The heralding efficiency is maximal for either loosely ($\xi_p < 0.001$) or very strongly focused spatial modes ($\xi_p \sim 10^2$). However, the utilization of smaller beam waists is associated with optical aberrations, larger bandwidths that can cause chromatic effects, and in general complicates the alignment. Tight focusing of the collection modes should therefore be avoided.

The pair collection efficiency is maximal for large confocal parameters ($\xi_p = \xi_s = \xi_i \sim 12$) and the parameters to optimize the brightness are the well known Boyd-Kleinman-parameters $\xi_p = \xi_s = \xi_i \sim 2.84$ [30].

It is to note though, that heralding efficiency, pair collection efficiency and spectral brightness cannot be maximized at the same time. For example the parameters providing maximal brightness would only allow for a heralding efficiency of 0.75, whereas for a high heralding efficiency of $\eta_h > 0.95$ the brightness would be reduced by a factor of 10.

As proposed for an ESA-funded project [34], a space suitable entangled photon source must provide a back-to-back coincidence rate of 10^6 counts per second to overcome atmospheric link losses. At the same time a visibility of >98% must be achieved, in order to guarantee a QBER smaller than 1% and thus a significant violation of Bell's inequality. As already pointed out, the heralding efficiency strongly affects the visibility for a given pair-rate. Hence, the choice of confocal parameter is subject to a trade off, which can also be influenced by spectral filtering.

5 High-heralding-efficiency Sagnac source

This chapter presents the experimental realization of the Sagnac-type source. An overview of the used devices is given, as well as a detailed discussion of the alignment process, which is crucial for the performance of the source.

5.1 Architecture of the source

An illustration of the experimental setup can be seen in figure 5.1. A photograph of the final source composition is shown in figure 5.2.

It is pumped by 405 nm linearly polarized light, produced by an UV-laser¹, which is placed on an external bread board. The pump beam is guided through a half-wave- and a quarter-wave-plate before it is coupled into a single-mode-fiber and led to the main source setup. In order to avoid resonant feedback a Faraday filter is placed after the laser output.

There, the beam is first collimated by a $f=4$ mm lens (L1) and then focused with a $f=500$ mm plano-convex lens (L2) into the center of the crystal (ppKTP type-II). After passing a dichroic mirror (DM), which is highly reflective for wavelengths around 810 nm and transparent for 405 nm under an incidence angle of 45° , it is separated at a polarizing beam splitter (PBS) to traverse the crystal in both directions.

¹ Omicron LDM-Serie-UV, operated in CW mode.

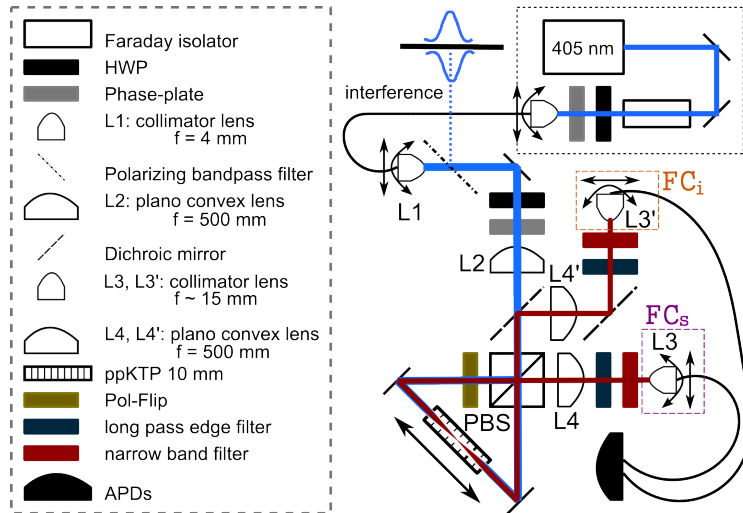


Figure 5.1: Schematic illustration of the Setup. The working principle and the used devices are listed in the text in section 5.1. FC_s and FC_i label the collection optics for signal and idler modes.



Figure 5.2: Photograph of the Sagnac loop setup. Instead of the usual HWP two periscopes were used to minimize beam aberrations and being able to also use the source for non-degenerate SPDC.

Beforehand the amplitudes of both pump directions are adjusted with a half-wave-plate (HWP).

The PBS lies at the heart of the setup, positioned in such a way, that incoming light will enter it in an almost 90° angle to the surface (arranged via back reflections). It is noteworthy though, that this incident angle does not have to be the one which allows for perfect extinction. Instead of a HWP two periscopes were used, one of them with parallel, the other with cross-faced mirrors, labelled as "Pol-flip" in figure 3.1. It was crucial to incident the mirrors of the periscope under a 45° angle, for a correct change of polarization. The whole setup was arranged in a way, that the pump beam, when traversing the setup, would "follow one line", meaning that the there and back beam should overlap perfectly. This was arranged by implementing an interferometer directly after decoupling the light to the setup stage. Therefore a polarizing band pass filter was positioned into the beam, transmitting horizontally and reflecting vertically polarized light. The functioning of this method will be elaborated on in the next section 5.2.

After a nonlinear interaction, the 810 nm SPDC photons exit the crystal collinearly in both directions, split again at the PBS and are then coupled into single-mode-fibers at signal-fiber-coupler (FC_s) and idler-fiber-coupler (FC_i) respectively. Those in turn are connected to twin APD-detectors. To shield the detectors from incoming UV-light and minimize the falsifying effects of stray light and fluorescence, long-pass edge filters² and additional narrow-band interference filters³ are placed in front of the collection modes. The detectors are connected with a multi-channel coincidence counting module, which can be used in combination with a home-made LabView software. This allows for setting the delay between the two collection channels, coincidence window and integration time.

For the best source performance three different methods for coupling the light were tested and compared:

² BLP01-647R-25 Semrock filters with a cut off at 647 nm

³ Semrock filters, T@810 nm > 90% with a FWHM bandwidth of 3.1 nm

1. **Configuration I:** Focusing into single mode fibers with Thorlabs $f=15.4$ mm aspheric lenses (L3, L3')
2. **Configuration II:** Collimating the SPDC-photons with $f=500$ mm plano-convex lenses (L4, L4')⁴ before coupling into SM-fibers
3. **Configuration III:** Collimating as in Configuration II and then focusing into SM-fibers with Schäfter Kirchhoff $f=15$ mm aspheric lenses (L3, L3')⁵.

In order to optimize the coupling later on, the focus lenses L4 and L4' were fastened on kinematic mounts with tip-tilt and x-y translation degrees of freedom.

5.2 Source-Alignment procedure

The quality, or rather the visibility of the intended entangled state is highly dependent on the indistinguishability of the created photons. This implies that any correlations between polarization- and other degrees of freedom, such as spectral, temporal or spatial, have to be eliminated. Only then a factorization of the state into a polarization- and spatio-temporal part is possible⁶.

Hence a major effort was dedicated to maximize the overlap of the spatial SPDC modes of both pump-directions. This was also important for efficient coupling into the SM-fibers.

In order to achieve this, the following alignment algorithm was performed:

1. Pump loop:

The pump beam was guided on a fixed height to the PBS. Then the periscopes were adjusted with the pump light. It was taken care that the angle of incidence was 45° onto the silver coated mirrors, to ensure a correct altering of

4 Thorlabs, LA1908-B BK7 B Coated Plano Convex

5 Schäfter+Kirchhoff 60FC-F-A15-02, with fine-focusing mechanism, AR-coated for 600-1050 nm.

6 Likewise for making use of other parameters for entanglement a decorrelation from all unused degrees of freedom is crucial.

the polarization plane. To adjust height and angles, the beam was guided through pinholes along the construction holes of the bread board. Hereafter the Sagnac-loop was completed by the two corner mirrors and both propagation directions overlapped. For coarse alignment the mirrors were moved until the pump was guided repeatedly through the pinholes on its way back. For precise alignment an interferometric measurement of the returning pump light was undertaken.

2. Inteferometric alignment:

For this purpose a polarizing band pass filter⁷ with a center wavelength at 405 nm was placed right after the exit of the pump into the source-setup (see figure 3.1). Under an incident angle of 45° it is only transmitting H- and reflecting V-polarized light. The intensity that was actually transferred to the setup was maximized by modulating the polarization by means of the QWP and HWP on the pump bread board. According to the setting of the subsequently positioned HWP, the Sagnac-loop is either pumped uni- or bidirectionally. By projecting the light to a white screen or a power-meter, one can exploit the following circumstance:

If the loop is pumped with equal intensities in clockwise and counterclockwise manner, and the beams, emerging from the two pump directions, spatially overlap perfectly, no light is reflected by the polarizing filter. In this case, the interfering beam is always H-polarized and thus entirely transmitted by the polarizing band-pass-filter⁸. Hence the intensity of the reflected light serves as indicator for the spatial overlap of the modes. A minimization of the intensity can be achieved by accurate setting of the HWP and precise adjustment of the mirrors of the Sagnac-interferometer, which is effectively equivalent to maximizing the spatial overlap.

⁷ 405/10 nm Semrock Polarizing Band pass filter, PBP01-405/10-25x36

⁸ For a detailed discussion please refer to section A.3

3. Signal- and idler loop:

Subsequently the signal and idler beam paths were overlapped with the pump. This was done by first back shining 635 nm laser light through the signal collection mode (FC_s) and guiding the beam with the adjustable mounts through the previously prepared pinholes. By removing the corner mirrors next to the periscopes of the Sagnac-interferometer, and matching the red and blue laser spots in a distance of 2 meters, a good overlap was confirmed. This was done for both propagation directions of the red laser light within the Sagnac loop, which was set beforehand by a polarizer. Thereafter the loop for the second (idler) collection mode (FC_i) was aligned the same way, with the difference that two dichroic mirrors were put into place to separate pump and infrared light, and direct the signal photons to the coupler. It was taken care that the dichroic mirrors were hit with an incidence angle of 45° , so the maximal infrared intensity would be reflected. Fine adjustments of both signal and idler loop were accomplished by reversing the polarization flip after the periscope with a HWP and coupling 808 nm light from one collection mode into the other fiber.

In order to adjust the beam waists of the pump and collection modes, a Spiricon CCD-camera⁹ was positioned with its photon sensitive area in the virtual crystal center. For the pump the plano convex lens was positioned such that the spots of minimal beam waist, when pumping the loop from both directions, matched in the center of the interferometer. With the beam shape analysing software provided by Spiricon, a Gauss-fit was performed and an actual pump beam waist of $200 \pm 40 \mu\text{m}$ measured, corresponding to a confocal parameter of $\xi_p=0.0146$.

Accordingly the collection modes were focused into the interferometer's center, yielding beam waists between 100 and 175 μm , which will be discussed in more detail in section 5.4. Figure 5.3 shows exemplary pictures taken with a CCD-camera of the pump, signal and idler beams in the virtual focus.

⁹ Spiricon LBA-FW-SCOR20 with IEEE-1394 connection

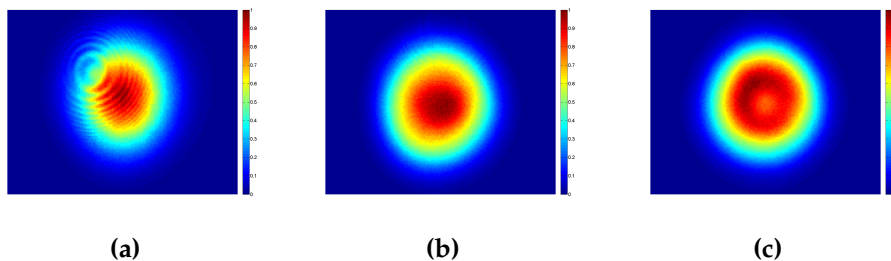


Figure 5.3: Pictures of the pump (a), signal (b) and idler (c) beams in the virtual focus of Configuration III. Due to the preserved Gaussian beam profile, it can be reasonably assumed that the optical devices show minor beam aberration producing effects. The distortion in (a) is presumably caused by the collimator that focused the beam in the crystal center.

Finally the ppKTP crystal, placed on a translation mount, was inserted into the center of the interferometer. Considering collinear SPDC-emission, the crystal was placed as straight as possible into the beam, with the phase matched axis aligned with the pump. This was done by looking onto the reflections of the UV-light on the transverse ends of the crystal. The crystal was tilted until both reflections appeared and disappeared simultaneously when moving the crystal in and out of the beam in x - and y -direction.

5.3 Source Performance characteristics

In this section the experimental results of the source efficiency and entanglement quality, as discussed in section 4, are presented. After fine-tuning the SPDC by means of alignment and temperature adjustments, the setup was optimized to yield maximal heralding efficiency. Once an ideal configuration was found, all further measurements regarding the performance were undertaken and analyzed.

5.3.1 Temperature setting

For type-II phasematching the center wavelengths of signal and idler mode change linearly with temperature. A measurement of the spectra over temperature can be seen in figure 5.5. The spectra were measured with a QE Pro high sensitivity spectrometer that provides a single-photon sensitivity of 90% and an optical resolution of 0.14 nm. A linear fit estimates a crystal temperature of about 31.7 °C for degenerate operation. However, the optimal value for high coincidence rates also depends on the transmission profile of the used filters, the wavelength dispersion of the used optical devices and so on, and might differ from the degenerate settings. Hence an additional temperature run during operation of the source was undertaken. It seemed that a temperature of 32 °C yielded the maximal coincidences, though it is to mention, that no significant change in coincidences was observed between 31 °C and 33 °C.

Figure 5.4 shows an exemplary spectrum of the signal mode at 32 °C. An applied Gaussian fit stated the FWHM to be $\sim 0.52 \text{ nm}^{10}$, which coincides perfectly with the prediction of approximation (4.8) for a 10 mm crystal.

5.4 Heralding efficiency

As discussed in section 4.1 the heralding efficiency is largely dependent on the focal parameters of the pump and collection optics. In order to experimentally implement the desired beam waists, the single-mode-fiber is imaged on the center of the crystal. This way the probability to collect down converted photons which are in a fundamental Gaussian mode is maximized. However, this only holds true if we assume that nothing in the setup will distort the beam shape or path in any way. Causes for such distortions could be misalignment, crystal- and/or other device imperfections. Furthermore, mechanical instabilities of the mounts could cause the coupling efficiency to be unstable in time.

¹⁰ From the Gaussian fit applied, the $FWHM = 2c1\sqrt{\ln 2}$

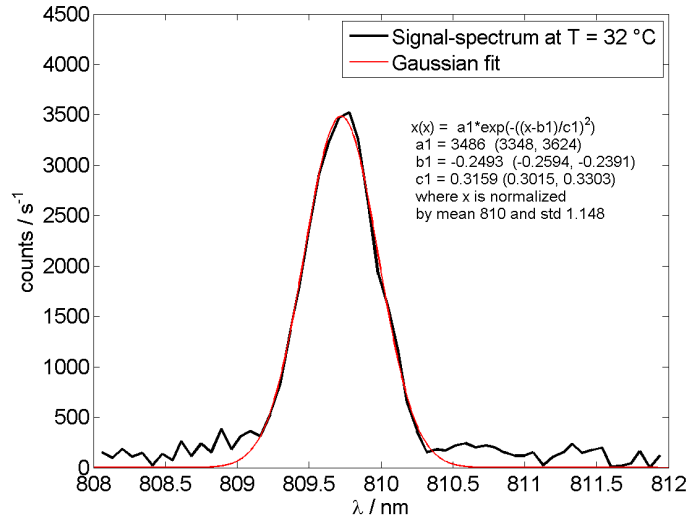


Figure 5.4: Exemplary spectrum, taken with the QEPro single photon spectrometer. It shows the signal-mode at 32 °C. The Gaussian fit states the FWHM to be ~ 0.52 nm.

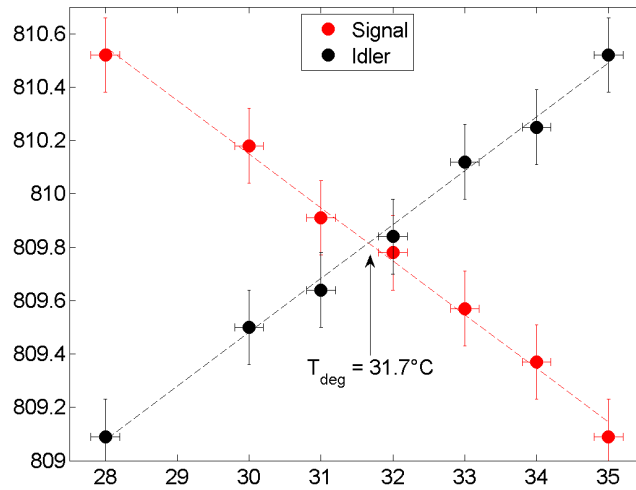


Figure 5.5: The signal and idler center wavelengths over temperature. The linear fit yields an optimal operation temperature of about 31.7 °C for degenerate emission.

	Configuration I	Configuration II	Configuration III
$\omega_p / \mu\text{m}$	200 ± 40	200 ± 40	200 ± 40
ξ_p	0.0146	0.0146	0.0146
$\omega_{s,i} / \mu\text{m}$	100 ± 10	75 ± 5	85 ± 5
$\xi_{s,i}$	0.13	0.21	0.16

Table 5.1: Observed beam waists and corresponding confocal parameters for three different optical configurations.

In order to achieve the highest possible heralding efficiency, three different coupling configurations for the collection channels were implemented and compared (see chapter 5.1). The resulting beam waists in the crystal center and the corresponding confocal parameters are listed in table 5.1.

According to the calculations pictured in figure 4.1a a combination of those confocal parameters for pump and collection modes is resulting in a heralding efficiency of almost 99%. The actually observed heralding efficiencies and the brightness of the source are summarized in table 5.2.

The heralding ratios were observed with an internal width of 4 of the TTM, implying an actual coincidence window of 11 ns. The mean pump power was 2 mW, measured right before the pump beam entered the PBS. The listed values for the heralding efficiencies are only corrected for dark counts, but not for any optical losses or detection efficiencies, thus no error is added. The fact that the values for heralding efficiency and brightness are balanced for all pump directions (except for configuration I) indicates a highly symmetric alignment.

The two-lens collection system (configuration II and III) seems to yield an improvement compared to utilization of just one aspheric lens to focus the down converted photons into the single mode fibers. The best results were obtained for configuration III, with heralding efficiencies of $\eta_{h,FC_s} = 0.42$ and $\eta_{h,FC_i} = 0.45$ for the signal and idler channel respectively. The asymmetry in heralding efficiencies is a consequence of dissimilar detection- and channel efficiencies. It is also to note that the connection

	η_{h,FC_s}	η_{h,FC_i}	brightness [cps/mW]	pump direction
Configuration I	0.33	0.39	2200	\Leftrightarrow
	0.33	0.39	2200	\Rightarrow
	0.35	0.42	2500	\Leftarrow
Configuration II	0.34	0.42	3000	\Leftrightarrow
	0.34	0.43	3000	\Rightarrow
	0.34	0.42	3100	\Leftarrow
Configuration III	0.42	0.45	3400	\Leftrightarrow
	0.42	0.45	3400	\Rightarrow
	0.42	0.45	3300	\Leftarrow

Table 5.2: Comparison of three different optical configurations (see chapter 5.1). Here the highest recorded heralding efficiencies for each configuration, as well as the brightness, are listed. The HWP setting denotes if the source was pumped in both directions (\Leftrightarrow), clockwise (\Rightarrow) or counterclockwise (\Leftarrow).

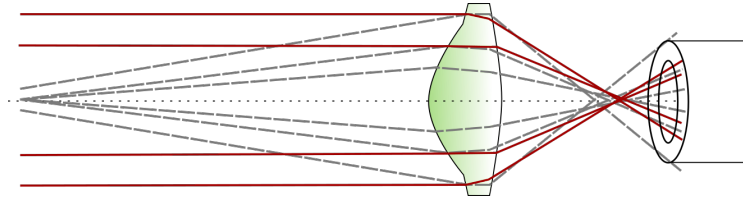


Figure 5.6: An aspheric lens is usually designed to correct lens aberrations, or to collimate a laser beam originating from a fiber. The sketch shows the difference between a divergent (gray, dash-dotted lines) and a collimated incident beam. The aspheric lens parameters are especially customized to provide a collimated beam, therefore divergence of the beam might lead to defocusing.

between the multi-mode-fibers of the detectors and the single-mode-fibers represented a source of error. The surfaces of the multi-mode-fiber-tips were scratched and due to slightly damaged threads, the connection was sometimes a little loose. The coupling efficiency was therefore very vulnerable to plugging and unplugging the fibers.

The enhancement between the one- and two-lens-system is most likely a consequence of improved performance of the aspheric coupling lens with a collimated incoming beam. The application of the aspheric lens usually aims to collimate a laser beam originating from a fiber and to correct for beam aberrations (see figure 5.6). However, if the incoming beam is divergent, aberrations might occur. Consequently, the coupling efficiency is reduced.

However, the observed values do not necessarily show the highest possible outcome, but rather reflect the maximum that could be achieved after putting a certain effort into the coupling process.

Loss estimation

The theoretically achievable heralding efficiency of $\sim 99\%$ is primarily limited by the detection efficiency and optical losses in the setup. An overall transmission of $\tau_{opt} \simeq 89\%$ by the optical components for a center wavelength of 810 nm was estimated by examination of the data sheets. Furthermore it is dependent on the

coupling efficiency into the single-mode-fibers, which depends on the one hand on a good overlap of SPDC- and the fiber-modes, on the other hand it is subject to alignment accuracy¹¹. The transmission of the SM-fibers was measured to be $\tau_{fiber} \sim 93\%$ for signal and idler channel. Additionally, any source that increases the single count rate, such as fluorescence or stray light will reduce the observed heralding efficiency. Furthermore a restricted polarization extinction ratio of the Sagnac loop will decrease the observed result, since it causes the photons to enter the wrong fiber and therefore increases the single count rate.

About 1% of the single counts could be attributed to fluorescence. This was evaluated by heating up the crystal to 64 °C. In that temperature region the signal- and idler-wavelengths are ~ 804 nm and ~ 816 nm respectively, and thus clearly outside the interference filter bandwidth. Any light that is still transmitted through the narrow band filters accounts therefore to fluorescence of the ppKTP or dPBS or to stray light.

The extinction ratio of the loop is mainly determined by the dPBS. By the manufacturer similar PBS-cubes were stated to have an extinction ratio of $T_p : T_s = 500:1$, with a transmission for the p-polarization of $T_p > 95\%$. However, this value was not attainable for all different incoming directions, but was merely limited to $T_p : T_s = 100:1$, when optimizing for all directions and polarizations.

In order to gain the actual heralding efficiency η_h the source is capable of, the following limiting factors have to be taken account for:

$$\eta_h = (\eta_{det} \times \tau_{opt,total})^{-1} \times \eta_{h,observed} \quad (5.1)$$

in particular the observed heralding efficiency $\eta_{h,observed}$, the transmittance of all optical devices $\tau_{opt,total}$, including the ppKTP crystal and the PBS, and the detection efficiency η_{det} of the SPADs. However, the fact that η_{det} is unknown, makes it infeasible to carry out reliable estimations for the heralding efficiency.

¹¹ The optimization of fiber-coupling is for example elaborated in [35].

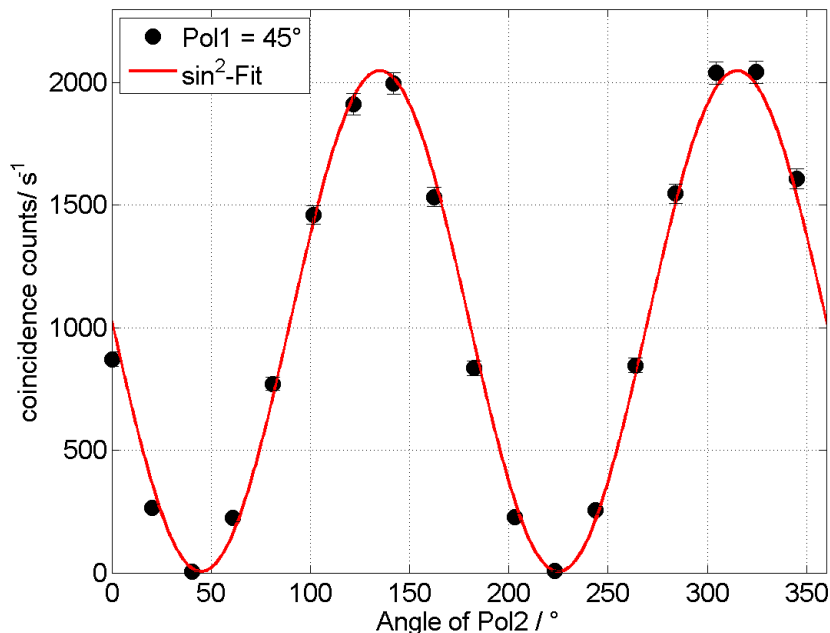


Figure 5.7: Exemplary results for a fringe visibility measurement for the $|\psi^-\rangle$ -state in the D/A-basis. It indicates $V_{D/A} = 99.5 \pm 0.2\%$. The experimental data points were fitted with a \sin^2 -curve.

5.5 Visibility

After optimizing the entangled photon source for high heralding efficiency, the output state was analyzed.

Hence two linear polarizers¹² were placed in front of the fiber couplers FC_s and FC_i . In order to prepare a $|\psi^-\rangle$ -state the polarizers were set both to $|D\rangle$ or $|A\rangle$. With this configuration no coincidences should be observable, hence the phase of the output state was adjusted by angle-tuning a thin bi-refringent plate about its optical axis. This allows the phase of the pump beam, and thus the entangled state, to be tuned without changing the magnitude of the H and V components of the pump

¹² Codixx colorPol® VISIR polarizer

$|\psi^-\rangle:$

Pol1	Pol2	R_s / cps	R_i / cps	R_c / cps
V	V	13400	8000	5
V	H	13400	7500	2700
H	H	10500	9300	8
H	V	12500	7200	2500
$V_{H/V} = 99.5 \pm 0.2 \%$				
A	A	13400	7200	5
A	D	13400	7800	3000
D	D	13200	7800	8
D	A	12500	7200	2200
$V_{D/A} = 99.5 \pm 0.2 \%$				

 $|\psi^+\rangle:$

Pol1	Pol2	R_s / cps	R_i / cps	R_c / cps
A	A	12000	7200	2500
A	D	11900	7600	12
D	D	12600	8000	2700
D	A	12400	7300	10
$V_{D/A} = 99.2 \pm 0.3 \%$				

Table 5.3: Measured single and coincidence counts for a $|\psi^-\rangle$ - and a $|\psi^+\rangle$ -target state. The values are corrected for dark counts, but not for accidental coincidences and correspond to high visibilities higher than 99 % for both states.

beam. The plate was tilted until a minimum coincidence count rate R_c was obtained. For preparing a $|\psi^+\rangle$ -state a crossed polarizer configuration would be needed to minimize the coincidence count rate.

To record the visibility fringes of the entangled state, the angle of the first polarizer was fixed, while the other polarizer was rotated in 20° -steps from 0° to 360° . The result of an exemplary measurement in the D/A-basis for a $|\psi^-\rangle$ -state can be seen in figure 5.7. The data points were fitted with a \sin^2 -function, according to equation (4.2) and indicate a visibility of $V_{D/A} = 99.5 \pm 0.2$.

As explained in section 3.1 there is an offset phase which usually has to be accounted for by phase-plate¹³. However, it turned out, that it was also possible to maximize the visibility for two Bell states requiring only adjustment of the HWP. A proper positioning of the HWP and the crystal, combined with symmetric alignment seemed to compensate already for this offset phase. Only the input polarization had to be changed between $|D\rangle$ and $|A\rangle$ to switch between a $|\psi^-\rangle$ and a $|\psi^+\rangle$ -state. Since recording the fringe visibility identically to figure 5.7 would require in total 72 different polarizer settings to analyze the two states in the H/V and D/A-basis respectively, only the coincidence maxima and minima were measured. Table 5.3 shows the raw data of such a visibility measurement, which was executed at a crystal temperature of 32°C while being pumped bidirectionally with ~ 1.8 mW on each side. After subtraction of dark counts an average single count rate of 13 kcps for the signal arm (FC_s) and 8 kcps for the idler arm (FC_i), as well as a maximal coincidence rate of 3 kcps could be obtained. The coincidences were measured in two conjugative bases, the H/V- and D/A-basis for the $|\psi^-\rangle$ -state, and additionally only in the D/A-basis for the $|\psi^+\rangle$ -state. The corresponding data in table 5.3 is corrected for dark counts but not for accidentals and implies high visibilities of $V_{|\psi^-\rangle} = 99.5 \pm 0.2\%$ and $V_{|\psi^+\rangle} = 99.2 \pm 0.3\%$ in the D/A-basis.

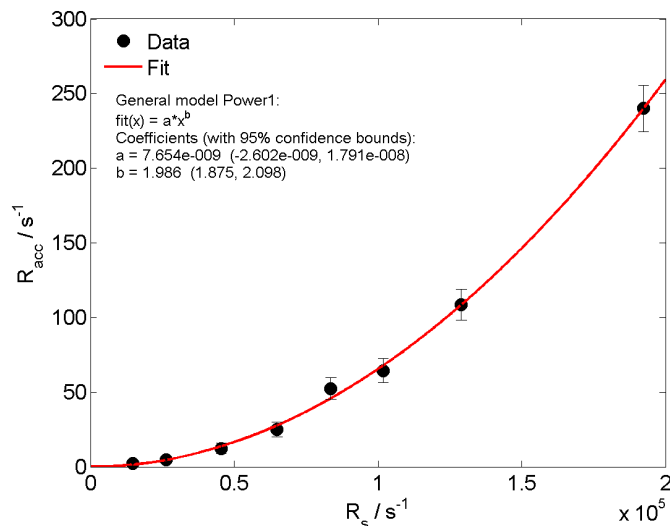


Figure 5.8: For increasing the amount of singles, the accidentals follow equation (A.5), with coefficient b agreeing very well with the mean coincidence window of ~ 11 ns.

5.5.1 Visibility at higher single rates

For a source to be applicable in space high pair rates are required. One method to increase the pair rate is using higher pump power. However, this has the disadvantage of producing more accidentals and consequently decreases the heralding efficiency and the visibility (see section A.1).

One way to experimentally evaluate the amount of accidentals is to set the delay between the signal- and idler channel in the time tagging software to a far-off value. Thus operation outside the delay histogram for the entangled photons is ensured and all coincidences can therefore be accredited to accidental counts. To ascertain if the used method is in accordance with the theory of section A.1, the single count rates were increased by increasing the pump power stepwise from 1.7 mW to 16 mW. The delay between both channels was set to ~ 61 ns, which is far off the correct delay of 25 ns. The data was recorded with an integration time of 10 s and a mean

¹³ Any birefringent material, which is transparent for the operational wavelength, can be used for this purpose.

coincidence window of 11 ns. Figure 5.8 shows the accidentals as a function of the "symmetric" singles, meaning the square root of signal- and idler-channel single counts $\sqrt{R_s R_i}$. The data was fitted with a power-function, reflecting equation (A.5). In accordance with the theory the accidentals increase as the square of the singles and coefficient $a \simeq 8 \pm 10$ ns coincides well with the actual mean coincidence interval of 11 ns.

To exploit the maximal possible amount of single counts with this system, the Omicron Laser was set to the highest possible value of 100 mW, resulting in an effective pump power of 12 mW for each pump direction. With polarizers in front of the couplers and with dark count subtraction, single count rates of $R_s \simeq 87$ kcps for the signal and $R_i \simeq 47$ kcps for the idler path were obtained. The mean amount of accidentals obtained experimentally was $R_{acc} = 40$ cps and fits well to the theoretical approximation of 45 cps. Table 5.4 shows a comparison between the observed visibilities for a $|\psi^-\rangle$ and a $|\psi^+\rangle$ -state with and without correction for accidentals. By subtracting the accidentals visibilities similar to those obtained for lower pump powers can be claimed. Certainly it is to mention, that correcting the raw data for accidentals is a delicate task. The outcome is highly dependent on the accidental-acquisition-method, whether it be theoretical or experimental, and is prone to adulterate the results in a positive way. Optimizing a source for high heralding efficiency might therefore be a possibility to circumvent this issue, since the coincidence rate is maximized for a given singles rate.

state	$V_{H/V}$	$V_{D/A}$
No accidentals subtracted		
$ \psi^-\rangle$	$98.5 \pm 0.4 \%$	$98.9 \pm 0.3 \%$
$ \psi^+\rangle$	$98.9 \pm 0.2 \%$	$99.0 \pm 0.2 \%$
Accidentals subtracted		
$ \psi^-\rangle$	$99.4 \pm 0.4 \%$	$99.4 \pm 0.3 \%$
$ \psi^+\rangle$	$99.7 \pm 0.2 \%$	$99.5 \pm 0.3 \%$

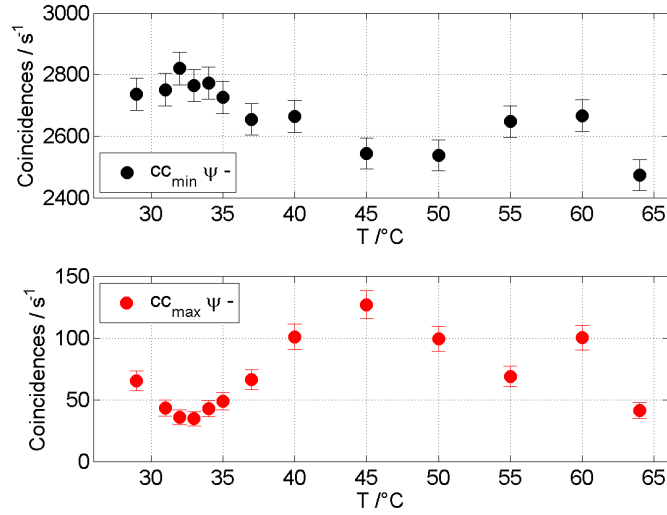
Table 5.4: Visibility for high single count rates with and without correction for accidentals.

6 Evaluation of phase stability

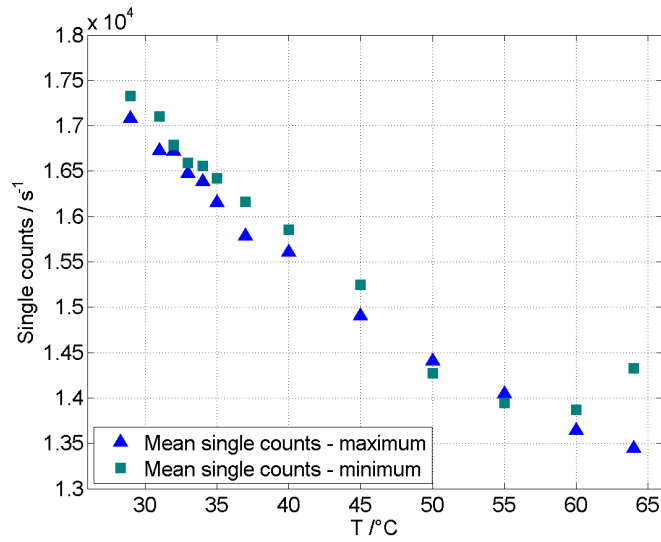
When putting a source for entangled photons into space one has to face more difficulties than running the setup in an earth bound lab. Since it is impossible to realign it once it is on a satellite, it has to be very stable and robust against environmental influences. For example temperature fluctuations become more relevant. From section 2.5.2 we can conceive that any changes in temperature will influence the output state. For a photon source to reliably provide a certain entangled state at the push of a button, the stability of the phase upon changes of the crystal, as well as environmental temperature is therefore a crucial issue. In this context the term "stable" implies that a visibility higher than 98% should be guaranteed.

To characterize the behaviour of the setup, the change of visibility with crystal temperature was analyzed. Since a full visibility measurement with this thesis' setup is very time consuming, we decided for a faster approach to investigate the stability of the phase upon large temperature changes. For this purpose we first used the minimum setting of the polarizers and measured the coincidences in 2 to 5 °C steps. In a second temperature run we proceeded likewise with the polarizers being in the maximum setting. This way a first impression of how the visibility will change with temperature could be acquired.

For the measurement the narrowband interference filters in front of the signal- and idler-couplers were removed and the phase of the state was adjusted roughly by the QWP in the pump beam to provide a $|\psi^-\rangle$ state at 32 °C. Then the temperature of the oven was scanned from 28 °C to 64 °C. For each step the coincidences were measured with an internal width of 2, corresponding to $\Delta\tau \sim 4.7$ ns, and integration



(a)



(b)

Figure 6.1: Figure (a) shows the coincidence minima and maxima over temperature. The visibility is maximal around 32°C and seems to increase again above 45°C until it reaches a local maximum around 55°C . The coincidences in the minimum setting could be affected by fluctuations in the mean single counts, as seen in (b). The blue triangles show the mean single counts collected by both fiber couplers for orthogonal polarizers and the green squares show the mean singles for crossed polarizers.

time of 5 s. Figure 6.1 shows the registered coincidences, that occurred for polarizer settings being in the minimum and maximum of the D/A-basis. The data points suggest the highest visibility around 32 °C of about 98% followed by a decrease up to 45 °C, where the visibility reaches a minimum of $\sim 89\%$. After this minimum the visibility seems to increase again though, until it reaches a local maximum around 55 °C. However, the data point at 60 °C might be an outlier, that can be accredited to fluctuations in mean single counts. In figure 6.1b one can see that above 55 °C the single counts for the minimum setting start to increase again, unlike the singles for the maximum setting. Nevertheless it is still to clarify what causes the drop-off in visibility.

The change in temperature entails a change in wavelength for signal and idler photons, but, as explained in section 3 the Sagnac-type-source is intrinsically compensating for those roots of distinguishability. A first guess for a reason for this instability was therefore improper alignment. As experienced during alignment and already pointed out for example in [36], also the position of the crystal inside the Sagnac loop is crucial for the output phase. Even though the SPDC photons are assumed to be created coherently and with equal probability over the length of the crystal, a change of the crystal position relative to the focus point results in a shift of time-delay distributions for both pump directions¹. It results from a group velocity mismatch for the orthogonally polarized photons and is simplistically visualized in figure 6.2. In [38] A. Predojević et. al. credit this position-dependent phase-shift in the output state mainly to dispersion in air and a Gouy phase that is acquired by the propagating Gauss-beams.

A simplistic way of visualizing it is the following: moving the crystal along the axis of beam propagation, the position of focus inside the crystal is changed. This is pictured in figure 6.2 for three different Gaussian beams with their waists located

¹ This is a direct result of the spatio-temporal correlations of the parametric down-conversion. The collection optics can be seen as a projection onto spatial modes with certain transverse momenta, which again are connected with a time delay between signal and idler. The time-delay distributions are shaped therefore by the collection-method-dependent distribution of transverse momenta, whereas the shift is given by the group-velocity-mismatch. For a more detailed description please refer to [37]

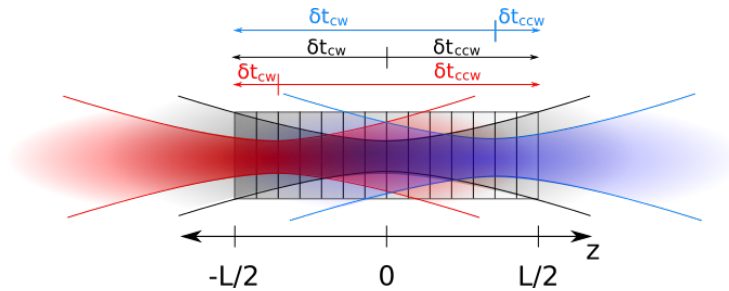


Figure 6.2: By moving the crystal the relative position of the focus of collection optics inside the crystal is changed. The black beam symbolizes a Gaussian with the waist in the crystal center, whereas the red and blue beams have their waists closer to the edges of the crystal. Assuming a maximum of the collected down-conversion-pairs originating from the focal point, the red and blue off-center positions result in different time-delays for clockwise (cw) and counterclockwise (ccw) propagation.

either in the center of the crystal or closer to the edges.

To check upon the effect of crystal position onto the phase-stability the coincidences over temperature were recorded for three different crystal positions. Similar to the prior measurements the polarizers in front of the fiber couplers were set parallel, in order to obtain a coincidence minimum. Crystal and oven were moved to three different spots along the propagation axis, denoted in figure 6.3 as z -positions of the translation mount's micrometer screw. The blue squares ($z = 8\text{mm}$) correspond to the crystal being in the center of the Sagnac loop, whereas the black circles ($z = 1\text{mm}$) and the red triangles ($z = 15\text{mm}$) correspond to the crystal being moved out of the center in clockwise and counterclockwise direction respectively. To compare the curves, the phase was adjusted roughly with a waveplate before each measurement run to a minimum at $32\text{ }^\circ\text{C}$. All measurements were done with the narrowband filters being removed, a pump power of $\sim 3\text{ mW}$, an internal width of 4 and the integration time set to 10 s.

If the instability of the phase with regard to the temperature-scan in figure 6.1 was a consequence of an off-center position of the crystal, one would expect the coincidence curve to flatten, while approaching the center. However, this is not what the results in figure 6.3 show. Around the minima at $30\text{ }^\circ\text{C}$ to $32\text{ }^\circ\text{C}$ the three

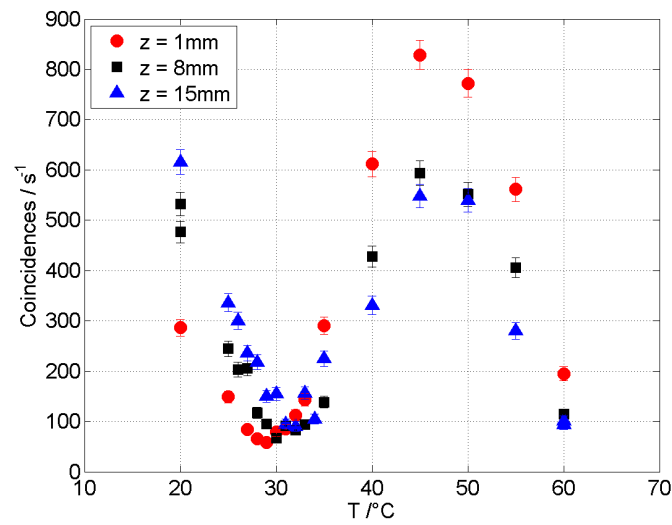


Figure 6.3: Coincidence minima over temperature for the crystal being moved to the center of the Sagnac loop (blue squares) and out of it (black circles, red triangles). For a position dependent phase-shift one would expect the curves to flatten at a centered position. Since this is not the case, the result could be a consequence of dispersion of some optical devices.

curves show a very similar increase. The decrease above 45 °C coincides again with an overall loss in counts and might therefore be not necessarily related to a phase shift. Having ruled out this influence a wavelength-dependent behaviour of at least one of the optical components in the setup has to be considered. For example the performance of the dPBS is sensitive to the operational wavelength and the angle of incidence. The wavelength-dependent phase shift between HV and VH could be explained by a polarization-dependent group-velocity dispersion in the multiple-layered coating of the center interface of the dPBS. For a more detailed description please refer to section A.4 in the appendix. However, it is as well conceivable that interchange of s- and p-polarization in the dielectric mirrors of the periscope leads to H and V photons experiencing different group-velocity dispersion depending on the propagation sense in the Sagnac loop. Furthermore imperfect alignment could result in slightly different center wavelengths and phase shifts for both clockwise and counter-clockwise propagation, thus rendering them distinguishable.

Even though these results prognosticate the visibility to be highly temperature dependent, the coincidence-minimum curve in figure 6.3 seems to only change slightly in a range of ± 5 °C around the maximum. This would imply a relatively stable visibility in that scope. To validate this, the visibility was measured in the H/V- and D/A-basis between 26 °C and 35 °C. The pump power was set to 3 mW, measured in front of the PBS, the integration time was again 5 s and the internal width = 2. The results can be seen in figure 6.4 and confirm that the visibility was indeed higher than 97 % between 26 °C and 31 °C. Due to the relatively small pump power the accidentals were not subtracted. From these results we conclude that a temperature stability to within ± 1 °C should be sufficient for reliable performance of a Sagnac-interferometer-based entangled photon source. This result is highly promising with regard to the development of a fully space-proof entangled photon source (which is currently being developed in collaboration with the European Space Agency).

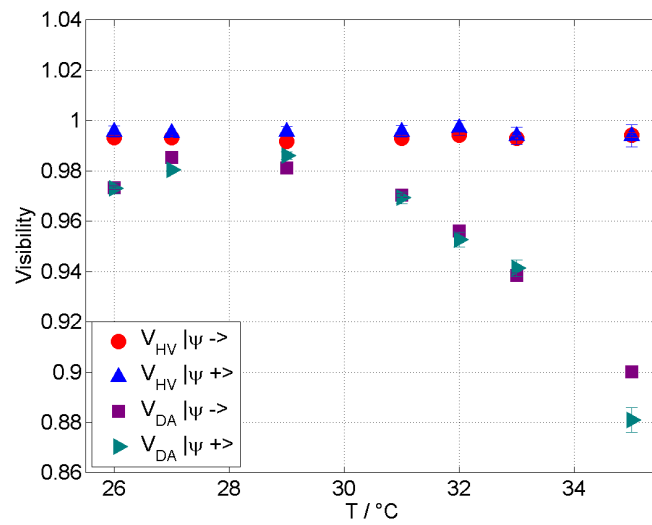


Figure 6.4: More effortful measurement of the visibility over temperature for a $|\psi^-\rangle$ - and a $|\psi^+\rangle$ -state for two mutually unbiased bases. The visibility in the D/A-basis is higher than 97% within a temperature range of $\Delta T = 5^\circ\text{C}$, while the visibility in the H/V-basis stays always higher than 99%.

6.1 Performance with multi-mode-fibers

In general the SPDC phase-matching gives rise to spatially multi-mode emission. By using single-mode-fibers we select only a small part of all emitted photon pairs. Furthermore coupling into single-mode-fibers is a delicate task and collection efficiency is prone to mechanical instabilities of the setup. Multi-mode-fibers on the contrary act as a kind of "bucket" for incoming light, which facilitates the coupling process and, due to acceptance of higher-order modes, leads to higher pair collection rates.

After connecting the multi-mode-fibers of the detectors directly to the source, mean single count rates of $R_s \sim 90$ kcps/mW and coincidence count rates of $R_c \sim 40$ kcps/mW could be observed. These values are ten times higher than the ones observed with single-mode-fibers. Thus, being able to exploit a much higher flux of entangled photons, it was interesting to evaluate the degree of entanglement. A visibility measurement for a $|\psi^-\rangle$ -state in the H/V- and D/A-basis was conducted. Table 6.1 lists the recorded data for a pump power of 1.4 mW, a crystal temperature of $T = 32$ °C and a coincidence time window of $\Delta\tau \simeq 11$ ns. Without correction for accidentals this data exhibits that the visibility in the H/V-basis was almost unchanged at $V_{H/V} = 99.0 \pm 0.1\%$, but in the D/A-basis reduced to $V_{D/A} = 92.5 \pm 0.2\%$.

For the observed values accidental counts of around 35 cps can be derived. Subtracting those from the raw data, the visibilities can be slightly increased to $V_{H/V} = 99.3 \pm 0.2\%$ and $V_{D/A} = 92.7 \pm 0.2\%$.

These results demonstrate that the polarization entanglement is largely decoupled from the spatial correlations, which were not experimentally verified within this thesis. However, we believe they can safely be implied, since the pump waist used to generate the SPDC photons was sufficiently large to be approximated as a collinear plane-wave throughout the SPDC interaction. Hence the transverse momenta of the signal and idler must be anti-correlated. Such simultaneous high correlations

Pol1	Pol2	R_s / cps	R_i / cps	R_c / cps
V	V	53000	68000	70
V	H	52000	63000	14400
H	H	57000	61000	75
H	V	51000	61000	15000
$V_{H/V} = 99.0 \pm 0.1 \%$				
A	A	49000	59000	550
A	D	50800	60000	13400
D	D	51000	60500	500
D	A	51200	60100	13600
$V_{D/A} = 92.5 \pm 0.2 \%$				

Table 6.1: Visibility measurement with multi-mode-fibers.

in multiple degrees of freedom are called "hyperentanglement"². Since this adds new dimensions to the Hilbert space of a qubit, which can be exploited as information carriers, hyperentanglement could provide promising applications in quantum information processing, for example in superdense teleportation [40] or hyperentanglement assisted deterministic Bell state tests [41, 42].

J. T. Barreiro et al. prove in [43] that entanglement in different degrees of freedom can, in general, be implemented in one photonic quantum system. Considering the shown alignment tolerances and the high symmetry of the Sagnac-architecture, this source represents a good candidate for a highly efficient source for hyperentanglement, with coincidence rates in the order of 40 kcps/mW shown in multi-mode operation.

² For an introduction to this topic the reader is, for example, referred to [39]

6.2 Performance with cross-spliced PM-fibers

Due to the fact that the information of the generated qubits is polarization encoded, it is very important to maintain this property until further processing takes place. Unfortunately it is a well known fact, that, by the virtue of mode-coupling, the polarization state fluctuates randomly along an optical fiber³. This disadvantage can theoretically be overcome by the utilization of cross-spliced polarization-maintaining (PM-) fibers of the same length instead of single-mode-fibers (For a short introduction to PM-fibers please refer to section A.5 in the appendix).

For cw-pumping we can assume symmetric deviations around the center-frequency for signal and idler:

$$\omega_p = (\omega_s + \Delta\omega) + (\omega_i - \Delta\omega) \quad (6.1)$$

Using only one fiber would thereby result in a relative phase-shift between signal and idler:

$$\exp [i\Delta\phi_{singlePM}] = \exp \left[iL\Delta\omega \left(\frac{1}{u_s} - \frac{1}{u_i} \right) \right] \quad (6.2)$$

where L denotes the length of the fiber and u_s and u_i the group velocities of signal and idler photon respectively. They depend on the ordinary and extraordinary refractive index of the fiber, which in return depends on the center-wavelength λ_0 of the propagating light:

$$u_{g_{s,i}} = \frac{c}{n_{o,e} - \lambda_{0_{s,i}} \frac{dn_{o,e}(\lambda_{0_{s,i}})}{d\lambda_{0_{s,i}}}} \quad (6.3)$$

³ It is to note, that this was not an issue for this thesis' experiments, since the polarization measurements took place before the photons entered the fibers, and those in turn were directly coupled to the detectors.

If the H-polarization is in the first fiber aligned with the fast axis, it experiences the extraordinary refractive index and V the ordinary. By adding a second PM-fiber of the same length and rotating it about 90° , ordinary and extraordinary refractive index for H and V are interchanged. Thus u_i and u_s are interchanged and the phase-shift acquired in the first fiber is effectively compensated:

$$\exp [i\Delta\phi_{crossedPM}] = \exp \left[i\Delta\omega \left(\left(\frac{1}{u_s} - \frac{1}{u_i} \right) + \left(\frac{1}{u_i} - \frac{1}{u_s} \right) \right) \right] = 1 \quad (6.4)$$

The high modal birefringence of the fibers is used to suppress the mode-coupling, and the perpendicular configuration is compensating for temporal walk-off as well as dispersive broadening. Thus the polarization should be maintained independent of input state and/or bandwidth. The interested reader may find further information in [44]. Here a similar approach is made, but with the difference that the fibers are used for a four-wave-mixing process, analogue to the crossed-crystal scheme [19].

To test the hypothesis two PM-fibers⁴ of one meter length were spliced together, with their optical axis perpendicular to each other. The performance upon change of input polarization and wavelength was then examined by measuring the polarization state after the fiber output with a polarimeter⁵.

The results for a center-wavelength scan between 805 and 811 nm for diagonally polarized classical input light⁶ are shown in figure 6.5. For better visualization the data is plotted in the Bloch-sphere representation. The blue spots correspond to data acquired with a single PM-fiber, whereas the red spots were obtained with the cross-spliced fiber. Using only a single PM-fiber led to a wavelength-dependent change in the output-polarization. This was expected, since the input state was not aligned with the optical axis of the fiber. H- and V-component of the polarization acquire therefore a relative phase shift, according to the wavelength-dependent refractive index of the fiber. The data points of the cross-spliced PM-

4 Nufern PM780-HP, Panda style

5 PAX5720IR1-T TXP free-space polarimeter for $\lambda = 700 - 1000$ nm

6 Generated by a grating stabilized IR-laser diode.

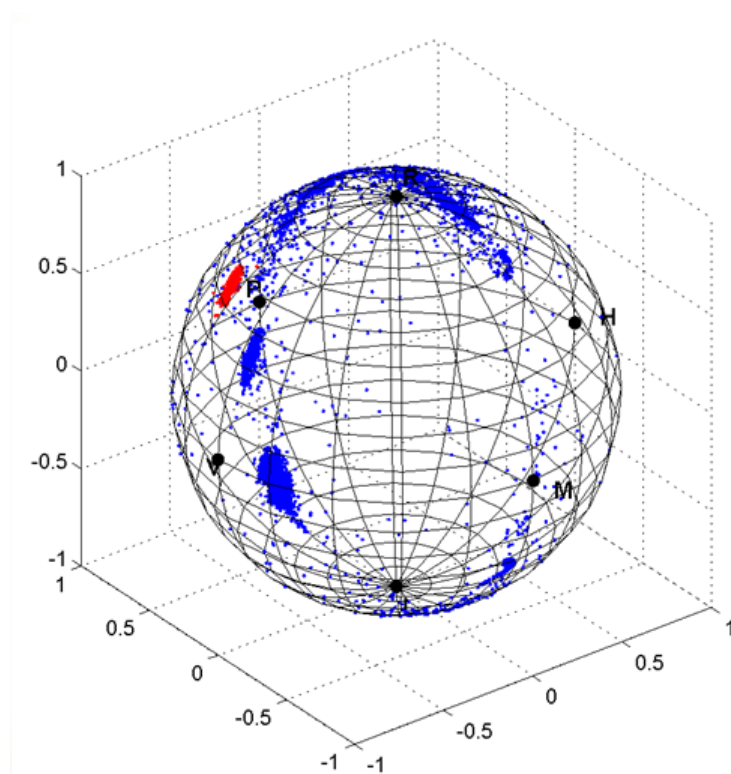


Figure 6.5: The polarization change upon wavelength change for a single PM-fiber (blue spots) and a crossed PM-fiber (red spots). The phase of the input state is held stable over the entire wavelength range for the crossed PM-fiber.

fiber are all concentrated close to the letter P on the Bloch-sphere, labeling the coordinate for diagonally ("Plus") polarized light. This indicates that the relative phase acquired by passing only one fiber could be well compensated by the second.

However, local temperature fluctuations have a severe impact on the birefringence of a PM-fiber (see for example [45]). The results were therefore subject to fluctuations already in the laboratory environment. For instance, the adjustment of the phase of the entangled state turned out to be infeasible, due to influences of body warmth, unequally affecting both parts of the spliced fiber. Thereupon further measurements with the cross-spliced PM-fibers were discontinued.

7 Conclusion and Outlook

Within this thesis I presented a source for polarization entangled photons, which was designed and characterized in the light of developing a source for operations on a satellite. Taking the atmospheric attenuation of an earth-satellite link into consideration, a key aspect of such a source is the efficiency of providing a desired entangled state, which is closely linked to a high heralding efficiency. The foci of pump and collection optics were selected in order to yield a high heralding efficiency of $\eta_h > 99\%$. Since η_h is depending on a good coupling efficiency, three different collection configurations were tested to increase it. The highest efficiencies of $\eta_{h,s} = 0.42$ and $\eta_{h,i} = 0.45$ were obtained by first collimating with a plano-convex lens and afterwards focusing the SPDC-photons with an aspheric lens into the single-mode-fibers. This can be explained by a better functioning of the aspheric lens with an incoming collimated beam. Since the detection efficiency of the used SPAD's is not known, the actual values are yet to specify. Hence, a next important step would be to measure the heralding efficiency with calibrated detectors, and this way avoid presumptions about the maximal value this source is capable of. In the following the setup can be refined by exchanging components that introduce losses, in particular the dPBS.

Another critical requirement for applications in space, as well as other out-of-the-lab operation conditions, is the reliability with which it produces a desired entangled state. Due to the symmetry of the configuration, the Sagnac loop scheme promises such stability, in particular with regard to drifts in crystal temperature, and pump wavelengths. This feature was experimentally corroborated and a degree of polarization entanglement higher than 99% was demonstrated in the H/V basis for

a temperature range of 5 °C. A less stable result was obtained for the D/A-basis, where, nevertheless, visibilities of more than 97% could be shown within the same scope.

It is very likely that dispersion of the used optical devices, such as the lenses or the PBS, restrict a possible higher phase stability for non-degenerate SPDC. Thus the wavelength dependency of all optical components has to be analyzed and replacements have to be implemented in the setup consequently.

To make the fiber-output intrinsically phase-stable, the idea of using cross-spliced PM-fibers instead of single-mode-fibers was tested. Although measurements with a polarimeter confirmed in general the functionality of this scheme for maintaining the polarization of signal and idler for arbitrary input states and bandwidths, the high sensitivity of the fiber's birefringence to local temperature fluctuations make it unfortunately rather uninteresting for space-applications.

Furthermore, the very symmetric architecture of the source allowed for producing two different Bell-states with high visibilities of more than 99% in two unbiased bases at constant crystal temperature.

Also visibility measurements with multi-mode-fibers yielded good results of more than 99% in the H/V- and 92% in the D/A-basis. This indicates strong correlations in the polarization, as well as in the spatial degree of freedom. These characteristics of the Sagnac could be exploited by auspicious hyperentanglement protocols, such as Superdense Teleportation or complete deterministic Bell-state analysis, but still wait for validation.

A Appendix

A.1 Effects of accidental coincidences

Accidental coincidences occur when two uncorrelated photons are erroneously counted as a coincidence. This can happen when one photon of the emitted pair is detected, but its partner gets lost. When within half of the coincidence time window (set by the time tagging software) another pair is created, and also only one photon gets lost, the two "surviving" photons are counted as a real coincidence. As we will see, this can lead to a degradation of entanglement visibility.

Assuming within the SPDC-process an average rate R_0 of photon pairs is emitted. However, even for perfect alignment, the optical setup and used devices are not ideal and the rate eventually acquired by the detectors is reduced by various reasons, such as:

- optical transmission losses,
- losses induced by the finite extinction of the polarizing beam splitter or other polarizing components,
- reduced detection efficiency of the APDs.

Those effects all sum up to an overall detection efficiency η , which might differ for the signal and idler channel. With this considerations, and negligence of dark counts, we can write the rate of single photon counts by the detector in the signal- and idler-channel as:

$$R_s = R_0\eta_s \quad (\text{A.1})$$

$$R_i = R_0\eta_i \quad (\text{A.2})$$

Without taking into account any accidentals yet, the rate of registered coincidences is then:

$$R_{c,0} = R_0\eta_s\eta_i\eta_h \quad (\text{A.3})$$

with η_h the heralding efficiency of the source (see section 5.4).

For distinguishable photon pairs (i. e. the coherence time of the photons is smaller than the coincidence window of the detection $t_{coh} < \Delta\tau$), the photon pairs are emitted with a Poissonian distribution [46]:

$$P_n \simeq e^{-\mu} \frac{\mu^n}{n!} \quad (\text{A.4})$$

with μ being the average number of produced photon pairs per coincidence window $\Delta\tau$. In this case the number of accidentals can be approximated by

$$R_{acc} \simeq R_s R_i \Delta\tau \quad (\text{A.5})$$

and the registered coincidence rate is increased by

$$R_c = R_{c,0} + R_{acc} \quad (\text{A.6})$$

To comprehend the impact on our measurement, we will now consider having prepared a maximally entangled $|\psi^-\rangle$ -state. The visibility of the state is measured with two polarizers in front of the detectors is

$$V = \frac{R_{c,orthogonal} - R_{c,parallel}}{R_{c,orthogonal} + R_{c,parallel}} \quad (\text{A.7})$$

with $R_{c,orthogonal}$ and $R_{c,parallel}$ being the coincidence counts for orthogonal and parallel polarizer constellations. For perfect alignment, the coincidences for parallel polarizers are only due to accidentals:

$$R_{c,parallel} \simeq R_{acc} \quad (\text{A.8})$$

and the visibility is approximately ¹:

$$V = \frac{R_c - R_{acc}}{R_c + R_{acc}} = \frac{R_{c,0}}{R_{c,0} + 2R_{acc}} \simeq \frac{1}{1 + \frac{2\mu}{\eta_h}} \quad (\text{A.9})$$

¹ Please note that for deriving these formulas, dark counts of the detectors were neglected.

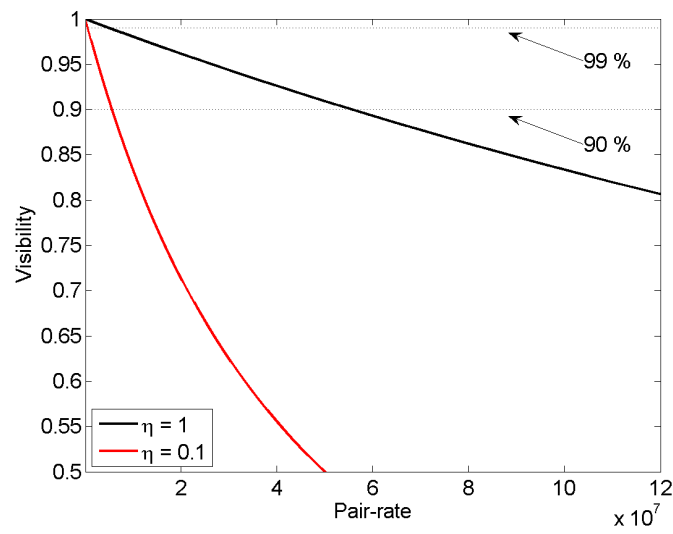


Figure A.1: Decrease of visibility for a perfectly entangled state with increasing pair-emission, simulated for unit heralding efficiency (black) and a low heralding efficiency (red), using a coincidence window of $\Delta\tau = 1$ ns. It is apparent, that at low heralding efficiency a lower pair-rate is sufficient for the visibility to drop under certain limits, as shown here for the exemplary values of 0.99 and 0.9 respectively.

A.2 Polarization flip with a cross-faced periscope

The interchange of H- and V-polarized light with the cross-faced periscope is due to a geometrical effect, which is illustrated in figure A.2b. For parallel mirrors p- and s-plane remain the same for both reflections, whereas for cross-faced mirrors s- and p-plane are interchanged. Within the chosen Cartesian coordinate system, the p-polarized light corresponds to vertical, and the s-polarized light to horizontal polarization. Considering now ideal mirrors with unit reflection coefficients for both s and p under a 45° angle of incidence, the cross-faced configuration will thus ultimately result in an interchange of H- and V-polarization.

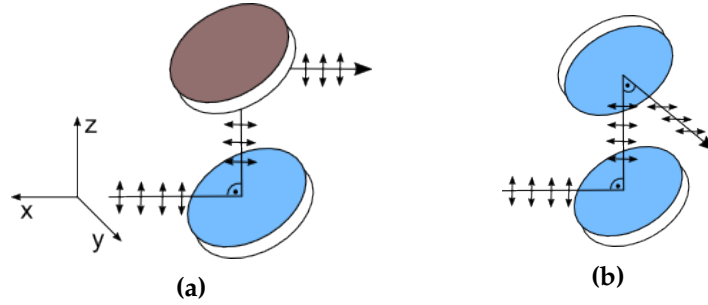


Figure A.2: Illustration of the "polarization-flip" by the periscope for initially s- or p-polarized light. Figure (a) shows the mirrors with their surfaces parallel to each other. The plane in which the electric field oscillates is not altered. Figure (b) shows the "flip". The plane of incidence is rotated about $\frac{\pi}{2}$ around the z-axis with respect to (a). In this reference frame the light is purely s-polarized.

A.3 Alignment interferometer

For explaining the functional principle of the alignment interferometer, we will use the Jones-formalism with the following definitions for the HWP and linear polarizations:

$$HWP(\theta) = \begin{pmatrix} \cos(2\theta) & \sin(2\theta) \\ \sin(2\theta) & -\cos(2\theta) \end{pmatrix} \quad (\text{A.10})$$

$$|H\rangle = \begin{pmatrix} 1 \\ 0 \end{pmatrix} \quad |V\rangle = \begin{pmatrix} 0 \\ 1 \end{pmatrix} \quad |D\rangle = \frac{1}{\sqrt{2}} \begin{pmatrix} 1 \\ 1 \end{pmatrix} \quad |A\rangle = \frac{1}{\sqrt{2}} \begin{pmatrix} 1 \\ -1 \end{pmatrix} \quad (\text{A.11})$$

with θ being the angle-setting of the fast axis.

In the following we assume perfect spatial overlap of the two propagation directions of the Sagnac-loop. After the polarizing band pass filter the pump light is H-polarized and its pass through the loop is affected by the following steps:

1. For an arbitrary HWP-setting $\alpha = 2\theta$ we get

$$\begin{pmatrix} \cos(\alpha) & \sin(\alpha) \\ \sin(\alpha) & -\cos(\alpha) \end{pmatrix} \begin{pmatrix} 1 \\ 0 \end{pmatrix} = \begin{pmatrix} \cos(\alpha) \\ \sin(\alpha) \end{pmatrix} \quad (\text{A.12})$$

2. The optical devices in the loop, including the lenses and phase-plate, will introduce a phase for the H- and V-component we don't know about, represented by the operator \hat{D} :

$$\hat{D} \begin{pmatrix} \cos(\alpha) \\ \sin(\alpha) \end{pmatrix} = \begin{pmatrix} \cos(\alpha)e^{i\phi_H} \\ \sin(\alpha)e^{i\phi_V} \end{pmatrix} \quad (\text{A.13})$$

3. The performance of the PBS together with the periscope is described by a flip of the H- and V-component:

$$\hat{P} \begin{pmatrix} \cos(\alpha)e^{i\phi_H} \\ \sin(\alpha)e^{i\phi_V} \end{pmatrix} = \begin{pmatrix} A \cdot \sin(\alpha)e^{i\phi_V} \\ B \cdot \cos(\alpha)e^{i\phi_H} \end{pmatrix} \quad (\text{A.14})$$

The prefactors A and B account for possibly differing transmission coefficients for the two propagation directions of the Sagnac-loop.

4. On the way back the same phase for H- and V-component is acquired:

$$\hat{D} \begin{pmatrix} A \cdot \sin(\alpha)e^{i\phi_V} \\ B \cdot \cos(\alpha)e^{i\phi_H} \end{pmatrix} = \begin{pmatrix} A \cdot \sin(\alpha) \\ B \cdot \cos(\alpha) \end{pmatrix} \cdot e^{i(\phi_H + \phi_V)} \quad (\text{A.15})$$

We see that there is no relative phase shift between the components, so we can neglect the global phase $\phi = \phi_H + \phi_V$ for the further calculations.

5. Arriving at the HWP from the other side now changes the angle of the fast axis to $\theta + \pi$ and thus to $\alpha + 2\pi = \alpha$:

$$H\hat{W}P(\alpha) \begin{pmatrix} A \cdot \sin(\alpha) \\ B \cdot \cos(\alpha) \end{pmatrix} = \begin{pmatrix} \sin(\alpha)\cos(\alpha)(A + B) \\ (A \cdot \sin^2(\alpha) - B \cdot \cos^2(\alpha)) \end{pmatrix} \quad (\text{A.16})$$

For $A=B$ the V-component vanishes for $\alpha = \pm 45^\circ$, which corresponds to the states $|D\rangle$ and $|A\rangle$, hence bidirectional pumping. For unidirectional pumping, corresponding to $\alpha = 0^\circ$ ($|H\rangle$) and $\alpha = 90^\circ$ ($|V\rangle$), the H-component vanishes and the loop acts as perfect isolator. Furthermore we can conclude from the result, that different transmission coefficients for clockwise and counterclockwise pumping, can be compensated by a convenient setting of the HWP-angle.

A.4 Polarizing Beam Splitter

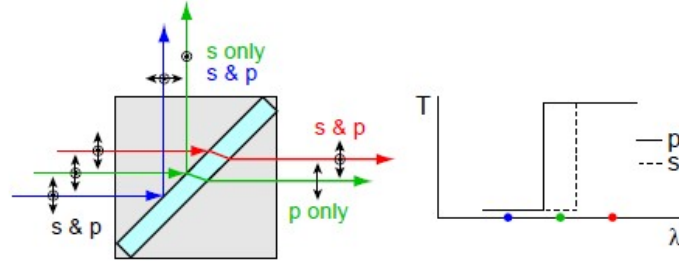


Figure A.3: A thin film polarizing beam splitter cube is only working in a small wavelength range. Above and below a spectral range it is either reflecting or transmitting both polarizations. Picture taken from [47].

A thin film polarizing beam splitter cube, as used for this thesis, basically consists of two cemented glass prisms, as can be seen in figure A.3. It is based on interference in a dielectric thin-film layer on the interface between the prisms, and is therefore only functioning in a small wavelength range. Usually the hypotenuse of one of the prisms is coated with a film that consists of multiple $\sim \lambda/4$ -layers. Hence it acts highly reflective under an incidence angle of 90° . However, for light incident under the Brewster angle²

$$\theta_B = \arctan\left(\frac{n_2}{n_1}\right) , \quad (\text{A.17})$$

only s-polarized light is reflected and p-polarized light transmitted. It depends solely on the refractive indices $n_{1,2}$ of the two involved materials. Therefore the components of the beam splitter cube can be chosen such that $\theta_b = 45^\circ$, which makes it very convenient for alignment.

² The Brewster angle is resulting from the Fresnel equations for reflected and transmitted intensity of electromagnetic waves upon incidence on a flat surface.

A.5 Polarization maintaining fibers



Figure A.4: Polarization-maintaining PANDA fiber (left) and bow-tie fiber (right). Introduced stress elements artificially increase the materials birefringence. Picture taken from [48].

In polarization maintaining fibres the birefringence is artificially increased to about $B = 10^{-4}$. The difference of the propagation constants for the two polarizations is thus enlarged. Hence, the relative phase between them drifts away rather fast, and regular disturbances throughout the fiber don't couple both modes anymore. However, this requires the incoming polarization to be aligned with one of the fiber's optical axes. The birefringence can be introduced by replacing the circular cross-section by an elliptical one, or introduce stress along one axis of the fiber, as is done in the "Panda-style" PM-fiber or the "Bow-tie"-fiber, as seen in figure A.4. The quality of a PM-fiber is measured with the extinction ratio:

$$ER = 10 \log \frac{P_{max}}{P_{min}} \quad (\text{A.18})$$

P_{max} and P_{min} are the intensities of the light after traversing a polarizer with orthogonal settings, measured in mW. Ideally extinction ratios of 40 dB or more would be needed to prevent any cross-talk between the polarizations.

B Error Analysis

The coincidence rates can be considered to follow a Poissonian distribution. The statistical uncertainty that inheres to them is therefore given by

$$\Delta R_c = \sqrt{R_c} \quad (\text{B.1})$$

For extracting the induced uncertainty in the visibilities conventional error propagation is used

$$\Delta V(R_{c,i}) = \sqrt{\sum_i \left(\frac{\partial V}{\partial R_{c,i}}\right)^2 \cdot (\Delta R_{c,i})^2} \quad (\text{B.2})$$

With the definition $N = \sum_i R_{c,i}$, the corresponding uncertainty is

$$\Delta V = \sqrt{\frac{1}{N}(1 - V^2)} \quad (\text{B.3})$$

Bibliography

- [1] Cheng-Zhi Peng, Jun Zhang, Dong Yang, Wei-Bo Gao, Huai-Xin Ma, Hao Yin, He-Ping Zeng, Tao Yang, Xiang-Bin Wang, and Jian-Wei Pan. Experimental long-distance decoy-state quantum key distribution based on polarization encoding. *Phys. Rev. Lett.*, 98:010505, Jan 2007. doi: 10.1103/PhysRevLett.98.010505. URL <http://link.aps.org/doi/10.1103/PhysRevLett.98.010505>.
- [2] Danna Rosenberg, Jim W. Harrington, Patrick R. Rice, Philip A. Hiskett, Charles G. Peterson, Richard J. Hughes, Adriana E. Lita, Sae Woo Nam, and Jane E. Nordholt. Long-distance decoy-state quantum key distribution in optical fiber. *Phys. Rev. Lett.*, 98:010503, Jan 2007. doi: 10.1103/PhysRevLett.98.010503. URL <http://link.aps.org/doi/10.1103/PhysRevLett.98.010503>.
- [3] Hiroki Takesue, Sae Woo Nam, Qiang Zhang, Robert H. Hadfield, Toshimori Honjo, Kiyoshi Tamaki, and Yoshihisa Yamamoto. Quantum key distribution over a 40-dB channel loss using superconducting single-photon detectors. *Nature Photonics*, 1(6):343–348, 2007. ISSN 1749-4885, 1749-4893. doi: 10.1038/nphoton.2007.75. URL <http://www.nature.com/doi/10.1038/nphoton.2007.75>.
- [4] C. Gobby, Z. L. Yuan, and A. J. Shields. Quantum key distribution over 122 km of standard telecom fiber. *Applied Physics Letters*, 84(19):3762, 2004. ISSN 00036951. doi: 10.1063/1.1738173. URL <http://scitation.aip.org/content/aip/journal/apl/84/19/10.1063/1.1738173>.
- [5] R. Ursin, F. Tiefenbacher, T. Schmitt-Manderbach, H. Weier, T. Scheidl, M. Lindenthal, B. Blauensteiner, T. Jennewein, J. Perdigues, P. Trojek, B. Ömer,

- M. Fürst, M. Meyenburg, J. Rarity, Z. Sodnik, C. Barbieri, H. Weinfurter, and A. Zeilinger. Entanglement-based quantum communication over 144 km. *Nature Physics*, 3(7):481–486, 2007. ISSN 1745-2473, 1745-2481. doi: 10.1038/nphys629. URL <http://www.nature.com/doifinder/10.1038/nphys629>.
- [6] Alessandro Fedrizzi, Rupert Ursin, Thomas Herbst, Matteo Nespoli, Robert Prevedel, Thomas Scheidl, Felix Tiefenbacher, Thomas Jennewein, and Anton Zeilinger. High-fidelity transmission of entanglement over a high-loss free-space channel. *Nature Physics*, 5(6):389–392, 2009. ISSN 1745-2473, 1745-2481. doi: 10.1038/nphys1255. URL <http://www.nature.com/doifinder/10.1038/nphys1255>.
- [7] Jean-Philippe Bourgoin, Brendon L. Higgins, Nick Gigov, Catherine Holloway, Christopher J. Pugh, Sarah Kaiser, Miles Cranmer, and Thomas Jennewein. Free-space quantum key distribution to a moving receiver. *arXiv*, May 2015. doi: arXiv:1505.00292. URL <http://arxiv.org/abs/1505.00292>.
- [8] Ana Rodríguez Aramendía. *Photonic entanglement exposed to high accelerations*, Master’s thesis, University of Vienna, to appear.
- [9] Pochi Yeh Amnon Yariv. *Photonics: Optical Electronics in Modern Communications*. Oxford University Press, Inc., 6th edition.
- [10] E. Schrödinger. Die gegenwärtige Situation in der Quantenmechanik. *Die Naturwissenschaften*, 23(49):823–828, 1935. ISSN 0028-1042. doi: 10.1007/BF01491914. URL <http://dx.doi.org/10.1007/BF01491914>.
- [11] G. Blatter. Quantenmechanik I, 2005. URL <http://www.itp.phys.ethz.ch/research/condmat/vortex/lectures/qm1>.
- [12] Maria Tenger. Photonic Qubits for Quantum Communication - Exploiting photon-pair correlations; from theory to applications, 2008. URL <http://www.diva-portal.org/smash/get/diva2:14014/FULLTEXT01.pdf>.
- [13] John S. Bell. On the Problem of Hidden Variables in Quantum Mechanics.

Bibliography

- Rev. Mod. Phys.*, 38:447–452, Jul 1966. doi: 10.1103/RevModPhys.38.447. URL <http://link.aps.org/doi/10.1103/RevModPhys.38.447>.
- [14] M. C. Teich B. E. A. Saleh. *Fundamentals of Photonics*. John Wiley & Sons, Inc., 2nd edition, 2007. ISBN 978-0-471-35832-9.
- [15] Single-photon generation and detection. In *Experimental Methods in the Physical Sciences*, volume 45, page iii. Elsevier, 2013. ISBN 9780123876959. URL <http://linkinghub.elsevier.com/retrieve/pii/B9780123876959000172>.
- [16] Juan P. Torres, K. Banaszek, and I.A. Walmsley. Engineering nonlinear optic sources of photonic entanglement. In *Progress in Optics*, volume 56, pages 227–331. Elsevier, 2011. ISBN 9780444538864. URL <http://linkinghub.elsevier.com/retrieve/pii/B9780444538864000058>.
- [17] V. A. Dyakov, V. V. Krasnikov, Vladimir I. Pryalkin, M. S. Pshenichnikov, T. B. Razumikhina, Vladimir S. Solomatin, and A. I. Kholodnykh. Sellmeier equation and tuning characteristics of KTP crystal frequency converters in the 0.4–4.0 μm range. *Soviet Journal of Quantum Electronics*, 18(9):1059–1060, 1988. ISSN 0049-1748. doi: 10.1070/QE1988v018n09ABEH012411. URL <http://stacks.iop.org/0049-1748/18/i=9/a=L01?key=crossref.0794574358ff316cb85685622f41c240>.
- [18] J. A. Armstrong, N. Bloembergen, J. Ducuing, and P. S. Pershan. Interactions between light waves in a nonlinear dielectric. *Phys. Rev.*, 127:1918–1939, Sep 1962. doi: 10.1103/PhysRev.127.1918. URL <http://link.aps.org/doi/10.1103/PhysRev.127.1918>.
- [19] Paul G. Kwiat, Klaus Mattle, Harald Weinfurter, Anton Zeilinger, Alexander V. Sergienko, and Yanhua Shih. New high-intensity source of polarization-entangled photon pairs. *Phys. Rev. Lett.*, 75(24):4337–4341, Dec 1995. doi: 10.1103/PhysRevLett.75.4337. URL <http://link.aps.org/doi/10.1103/PhysRevLett.75.4337>.
- [20] Paul G. Kwiat, Edo Waks, Andrew G. White, Ian Appelbaum, and Philippe H. Eberhard. Ultrabright source of polarization-entangled photons. *Phys. Rev.*

Bibliography

- A*, 60(2):R773–R776, Aug 1999. doi: 10.1103/PhysRevA.60.R773. URL <http://link.aps.org/doi/10.1103/PhysRevA.60.R773>.
- [21] Fabian Steinlechner, Pavel Trojek, Marc Jofre, Henning Weier, Daniel Perez, Thomas Jennewein, Rupert Ursin, John Rarity, Morgan W. Mitchell, Juan P. Torres, Harald Weinfurter, and Valerio Pruneri. A high-brightness source of polarization-entangled photons optimized for applications in free space. *Opt. Express*, 20(9):9640–9649, Apr 2012. doi: 10.1364/OE.20.009640. URL <http://www.opticsexpress.org/abstract.cfm?URI=oe-20-9-9640>.
- [22] Fabian Steinlechner, Sven Ramelow, Marc Jofre, Marta Gilaberte, Thomas Jennewein, Juan. P. Torres, Morgan W. Mitchell, and Valerio Pruneri. Phase-stable source of polarization-entangled photons in a linear double-pass configuration. *Opt. Express*, 21(10):11943–11951, May 2013. doi: 10.1364/OE.21.011943. URL <http://www.opticsexpress.org/abstract.cfm?URI=oe-21-10-11943>.
- [23] Marco Fiorentino, Gaétan Messin, Christopher E. Kuklewicz, Franco N. C. Wong, and Jeffrey H. Shapiro. Generation of ultrabright tunable polarization entanglement without spatial, spectral, or temporal constraints. *Phys. Rev. A*, 69(4):041801, Apr 2004. doi: 10.1103/PhysRevA.69.041801. URL <http://link.aps.org/doi/10.1103/PhysRevA.69.041801>.
- [24] Taehyun Kim, Marco Fiorentino, and Franco N. C. Wong. Phase-stable source of polarization-entangled photons using a polarization Sagnac interferometer. *Phys. Rev. A*, 73(1):012316, Jan 2006. doi: 10.1103/PhysRevA.73.012316. URL <http://link.aps.org/doi/10.1103/PhysRevA.73.012316>.
- [25] Alessandro Fedrizzi. *Fundamental experiments with a high brightness source of entangled photons*. Ph.D. thesis, University of Vienna, 2008.
- [26] Otfried Gühne and Géza Tóth. Entanglement detection. *Physics Reports*, 474(1):1–75, Apr 2009. ISSN 03701573. doi: 10.1016/j.physrep.2009.02.004. URL <http://linkinghub.elsevier.com/retrieve/pii/S0370157309000623>.
- [27] Daniel F. V. James, Paul G. Kwiat, William J. Munro, and Andrew G. White. Measurement of qubits. *Phys. Rev. A*, 64(5):052312, Oct 2001. doi: 10.1103/

Bibliography

- PhysRevA.64.052312. URL <http://link.aps.org/doi/10.1103/PhysRevA.64.052312>.
- [28] Alessandro Fedrizzi, Thomas Herbst, Andreas Poppe, Thomas Jennewein, and Anton Zeilinger. A wavelength-tunable fiber-coupled source of narrow-band entangled photons. *Opt. Express*, 15(23):15377–15386, Nov 2007. doi: 10.1364/OE.15.015377. URL <http://www.opticsexpress.org/abstract.cfm?URI=oe-15-23-15377>.
- [29] Ryan S. Bennink. Optimal collinear gaussian beams for spontaneous parametric down-conversion. *Phys. Rev. A*, 81:053805, May 2010. doi: 10.1103/PhysRevA.81.053805. URL <http://link.aps.org/doi/10.1103/PhysRevA.81.053805>.
- [30] G. D. Boyd and D. A. Kleinman. Parametric Interaction of Focused Gaussian Light Beams. *Journal of Applied Physics*, 39(8):3597, 1968. ISSN 00218979. doi: 10.1063/1.1656831. URL <http://scitation.aip.org/content/aip/journal/jap/39/8/10.1063/1.1656831>.
- [31] Fu-Yuan Wang, Bao-Sen Shi, and Guang-Can Guo. Generation of narrow-band photon pairs for quantum memory. *Optics Communications*, 283(14):2974–2977, 2010. ISSN 00304018. doi: 10.1016/j.optcom.2010.02.042. URL <http://linkinghub.elsevier.com/retrieve/pii/S0030401810001902>.
- [32] Christian Kurtsiefer, Markus Oberparleiter, and Harald Weinfurter. High-efficiency entangled photon pair collection in type-ii parametric fluorescence. *Phys. Rev. A*, 64:023802, Jul 2001. doi: 10.1103/PhysRevA.64.023802. URL <http://link.aps.org/doi/10.1103/PhysRevA.64.023802>.
- [33] Andrzej Dragan. Efficient fiber coupling of down-conversion photon pairs. *Phys. Rev. A*, 70:053814, Nov 2004. doi: 10.1103/PhysRevA.70.053814. URL <http://link.aps.org/doi/10.1103/PhysRevA.70.053814>.
- [34] Rupert Ursin, Fabian Steinlechner, Erik Beckert, and Oliver De Vries. Photonic Transceiver for Secure Space Communications: New Space Suitable Entangled Photon Source: Technical Note 2 - Optical design, 2015.

- [35] Fabian Steinlechner. *Towards a Loophole-Free Demonstration of EPR Nonlocality*, Master's thesis, Vienna University of Technology, 2010.
- [36] Deny R. Hamel. Realization of novel entangled photon sources using periodically poled materials. Oct 2010. URL <https://uwspace.uwaterloo.ca/handle/10012/5575>.
- [37] A. Büse, N. Tischler, M. L. Juan, and G. Molina-Terriza. Where are photons created in parametric down-conversion? on the control of the spatio-temporal properties of biphoton states. *J. Opt.*, 17(6):065201, Jun 2015. ISSN 2040-8986. doi: 10.1088/2040-8978/17/6/065201. URL <http://iopscience.iop.org/2040-8986/17/6/065201>.
- [38] Ana Predojević, Stephanie Grabher, and Gregor Weihs. Pulsed sagnac source of polarization entangled photon pairs. *Opt. Express*, 20(22):25022–25029, Oct 2012. doi: 10.1364/OE.20.025022. URL <http://www.opticsexpress.org/abstract.cfm?URI=oe-20-22-25022>.
- [39] Paul G. Kwiat Julio T. Barreiro. Hyperentanglement for advanced quantum communication. *Quantum Communications and Quantum Imaging VI*, Vol. 7092:9, 2008. doi: 10.1117/12.793513. URL <http://spie.org/Publications/Proceedings/Paper/10.1117/12.793513>.
- [40] Trent M. Graham, Herbert J. Bernstein, Tzu-Chieh Wei, Marius Junge, and Paul G Kwiat. Superdense teleportation using hyperentangled photons. *Nature Communications*, 6:7185, May 2015. ISSN 2041-1723. doi: 10.1038/ncomms8185. URL <http://www.nature.com/doifinder/10.1038/ncomms8185>.
- [41] M. Barbieri, G. Vallone, P. Mataloni, and F. De Martini. Complete and deterministic discrimination of polarization bell states assisted by momentum entanglement. *Phys. Rev. A*, 75:042317, Apr 2007. doi: 10.1103/PhysRevA.75.042317. URL <http://link.aps.org/doi/10.1103/PhysRevA.75.042317>.
- [42] Carsten Schuck, Gerhard Huber, Christian Kurtsiefer, and Harald Weinfurter. Complete deterministic linear optics bell state analysis. *Phys. Rev. Lett.*, 96:

Bibliography

- 190501, May 2006. doi: 10.1103/PhysRevLett.96.190501. URL <http://link.aps.org/doi/10.1103/PhysRevLett.96.190501>.
- [43] Julio T. Barreiro, Nathan K. Langford, Nicholas A. Peters, and Paul G. Kwiat. Generation of Hyperentangled Photon Pairs. *Phys. Rev. Lett.*, 95:260501, Dec 2005. doi: 10.1103/PhysRevLett.95.260501. URL <http://link.aps.org/doi/10.1103/PhysRevLett.95.260501>.
- [44] Evan Meyer-Scott, Vincent Roy, Jean-Philippe Bourgoin, Brendon L. Higgins, Lynden K. Shalm, and Thomas Jennewein. Generating polarization-entangled photon pairs using cross-spliced birefringent fibers. *Opt. Express*, 21(5):6205–6212, Mar 2013. doi: 10.1364/OE.21.006205. URL <http://www.opticsexpress.org/abstract.cfm?URI=oe-21-5-6205>.
- [45] Filip Dvorak, Jan Maschke, and Cestmir Vlcek. The response of polarization maintaining fibers upon temperature field disturbance. 12(2). ISSN 1804-3119, 1336-1376. doi: 10.15598/aeee.v12i2.1084. URL <http://advances.utc.sk/index.php/AEEE/article/view/1084>.
- [46] Hiroki Takesue and Kaoru Shimizu. Effects of multiple pairs on visibility measurements of entangled photons generated by spontaneous parametric processes. *Optics Communications*, 283(2):276 – 287, 2010. ISSN 0030-4018. doi: <http://dx.doi.org/10.1016/j.optcom.2009.10.008>. URL <http://www.sciencedirect.com/science/article/pii/S0030401809009651>.
- [47] Semrock, *a new class of polarization optics designed specially for lasers*. URL <http://www.semrock.com/a-new-class-of-polarization-optics-designed-specifically-for-lasers.aspx>.
- [48] *RP Photonics Encyclopedia*. URL https://www.rp-photonics.com/polarization_maintaining_fibers.html.

8 Acknowledgements

First and foremost I want to express my sincere gratitude to Dr. Rupert Ursin, not only for giving me the opportunity to work in such an exceptional place for science, but also for sharing his enthusiasm and motivation.

Further, I am deeply grateful to Fabian Steinlechner for his scientific guidance and ever open office door, notwithstanding the fact that he was usually assailed with questions by several students simultaneously.

I would also like to thank my other co-workers at IQOQI who made my time there so enjoyable and inspiring, especially my fellow "free-spacers", including Ana Rodríguez Aramendía, Matthias Fink, Johannes Handsteiner, Thomas Herbst, Sebastian Neumann and Sebastian Ecker¹. It was a great honour and fun to work and discuss with all of you!

Many thanks are due to Prof. Wolfgang Ernst for supervising me despite the spatial separation and organising everything in Graz.

Thank you Sabine and Alex for giving me shelter when needed.

I also owe gratitude to all my friends who kept me mentally healthy throughout the writing process by enduring my whining - particularly Eva and Sabine.

Finally, I want to thank my parents for their love and support in all that I do and my brother Stefan for being the person he is.

¹ The order of names was provided by a random number generator.